

The γ -ray deposition histories of core-collapse supernovae

Amir Sharon^{1*} and Doron Kushnir¹

¹*Dept. of Particle Phys. & Astrophys., Weizmann Institute of Science, Rehovot 76100, Israel*

Accepted XXX. Received YYY; in original form ZZZ

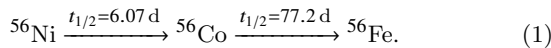
ABSTRACT

The γ -ray deposition history in an expanding supernova (SN) ejecta has been mostly used to constrain models for Type Ia SN. Here we expand this methodology to core-collapse SNe, including stripped envelope (SE; Type Ib/Ic/IIb) and Type IIP SNe. We construct bolometric light curves using photometry from the literature and we use the Katz integral to extract the γ -ray deposition history. We recover the tight range of γ -ray escape times, $t_0 \approx 30$ –45 d, for Type Ia SNe, and we find a new tight range $t_0 \approx 80$ –140 d, for SE SNe. Type IIP SNe are clearly separated from other SNe types with $t_0 \gtrsim 400$ d, and there is a possible negative correlation between t_0 and the synthesized ^{56}Ni mass. We find that the typical masses of the synthesized ^{56}Ni in SE SNe are larger than those in Type IIP SNe, in agreement with the results of Kushnir. This disfavors progenitors with the same initial mass range for these explosions. We recover the observed values of ET , the time-weighted integrated luminosity from cooling emission, for Type IIP, and we find hints of non-zero ET values in some SE SNe. We apply a simple γ -ray radiation transfer code to calculate the γ -ray deposition histories of models from the literature, and we show that the observed histories are a powerful tool for constraining models.

Key words: supernovae: general -gamma-rays: general -methods: data analysis

1 INTRODUCTION

It is widely accepted that the light curves of both Type Ia supernovae (SNe) and, at least for late times, core-collapse SNe, including stripped envelope (SE; Type Ib/Ic/IIb) and Type IIP SNe, are powered by the decay of radionuclides synthesized in the explosion. The most important power source is the decay chain (Pankey 1962; Colgate & McKee 1969)



The decay products consist of γ -rays and positrons, which transfer their energy to the expanding ejecta and heat it. This thermal energy is emitted as photons ranging from the infrared (IR) to ultraviolet (UV) that produce the bolometric luminosity of the SN, $L(t)$, where t is the time since explosion. The γ -ray optical depth is high shortly following the explosion, such that all the γ -ray energy is deposited within the ejecta. As the ejecta expands, the γ -ray optical depth decreases, and some γ -rays only partially deposit their energy, or just escape without interacting with the ejecta (Jeffery 1999). These γ -ray photons are usually not observed, with the exceptions of a handful of nearby SNe (Matz et al. 1988; Churazov et al. 2014). As the ejecta becomes optically thin, the bolometric luminosity equals the deposited energy,

$$L(t) = Q_{\text{dep}}(t), \quad (2)$$

such that the fraction of deposited γ -ray energy has a significant impact on the shape of the bolometric light curve. The deposited energy is given by

$$Q_{\text{dep}}(t) = Q_{\gamma}(t)f_{\text{dep}}(t) + Q_{\text{pos}}(t), \quad (3)$$

where $Q_{\gamma}(t)$ and $Q_{\text{pos}}(t)$ are the radioactive energy generated from γ -ray photons and the kinetic energy of positrons, respectively. The γ -ray deposition function, $f_{\text{dep}}(t)$, describes the fraction of the generated γ -ray energy deposited in the ejecta. We limit our analysis to times for which the kinetic energy of the positrons is deposited locally and instantaneously (Colgate et al. 1980; Ruiz-Lapuente & Spruit 1998; Milne et al. 1999; Kushnir & Waxman 2020) and for which the contribution from other decay channels (Seitenzahl et al. 2009) is negligible. The rest-mass energy of the positrons is emitted as γ -ray photons, which are included in $Q_{\gamma}(t)$. The energy generation rates of the γ -rays and of the positrons are (Swartz et al. 1995; Junde 1999):

$$Q_{\gamma}(t) = \frac{M_{\text{Ni}56}}{M_{\odot}} \left[6.54 e^{-\frac{t}{8.76\text{ d}}} + 1.38 e^{-\frac{t}{111.4\text{ d}}} \right] \times 10^{43} \text{ erg s}^{-1}. \quad (4)$$

and

$$Q_{\text{pos}}(t) = 4.64 \frac{M_{\text{Ni}56}}{M_{\odot}} \left[e^{-\frac{t}{111.4\text{ d}}} - e^{-\frac{t}{8.76\text{ d}}} \right] \times 10^{41} \text{ erg s}^{-1}, \quad (5)$$

where $M_{\text{Ni}56}$ is the mass of ^{56}Ni and all its radioactive parents at the time of the explosion. For a small enough γ -ray optical depth, each γ -ray photon has a small chance of colliding with matter from the ejecta (and a negligible chance for additional collisions), such that the deposition function is proportional to the column density, which scales as t^{-2} , and is given by (Jeffery 1999):

$$f_{\text{dep}}(t) = \frac{t_0^2}{t^2}, \quad \text{for } f_{\text{dep}} \ll 1, \quad (6)$$

where t_0 is the γ -ray escape time. The time t_c , for which the γ -rays deposited energy equals the positrons deposited energy, $Q_{\gamma}f_{\text{dep}} = Q_{\text{pos}}$, is given by Equations (4-6) as $t_c \approx$

* E-mail: amir.sharon@weizmann.ac.il

$5t_0$. For times when $t > t_c$, the main heating source of the ejecta is the kinetic energy loss of the positrons (Arnett 1979; Axelrod 1980).

The bolometric or pseudo-bolometric light curves of Type Ia SNe have been extensively studied in the past (see e.g. Branch & Tammann 1992; Milne et al. 2001). A common method to infer the ejecta properties of ^{56}Ni powered SNe is the analytical model of Arnett (Arnett 1979; Arnett 1982). In this model, the peak bolometric luminosity equals the instantaneous energy deposition rate at the peak time. This method is easy to implement and allows an estimate of the ejecta properties. However, the derivation of this ‘Arnett’s rule’ includes some simplifying assumptions, such as constant opacity and a uniform-heating-to-energy-density ratio, which do not hold for some ejecta profiles (Dessart et al. 2016; Khatami & Kasen 2019). As a result, the uncertainty in the estimated properties using ‘Arnett’s rule’ is hard to quantify.

The γ -ray escape time t_0 has been measured for Type Ia SNe (Stritzinger et al. 2006; Scalzo et al. 2014), by fitting the luminosity at late times under the assumption $L(t) = Q_{\text{dep}}(t)$ (*the direct method*). In order to include a transition between the γ -ray optically thick and thin regions, an interpolating function was used for $f_{\text{dep}}(t)$ (Jeffery 1999):

$$f_{\text{dep}}(t) = 1 - e^{-t_0^2/t^2}, \quad (7)$$

which provides the correct expressions for both regions. However, since the assumption $L(t) = Q_{\text{dep}}(t)$ is most valid for times where $f_{\text{dep}} \approx (t_0/t)^2$, then $Q_\gamma \propto M_{\text{Ni}56}t_0^2$, and there is a degeneracy between $M_{\text{Ni}56}$ and t_0 . In order to remove this degeneracy, observations with $t \gtrsim t_c$, for which the positrons contribution is significant, are required.

A different approach to measure t_0 is based on the Katz integral (Katz et al. 2013),

$$\int_0^t Q_{\text{dep}}(t')t'dt' = \int_0^t L(t')t'dt' + t'E(t')|_0^t, \quad (8)$$

where $E(t)$ is the (radiation-dominated) thermal energy of the ejecta gas. This relation is accurate for a non-relativistic expanding ejecta, independent of the assumption $L(t) = Q_{\text{dep}}(t)$. For Type Ia SNe, the term $tE(t)$ is small for both early and late times, such that for times when $L(t) = Q_{\text{dep}}(t)$, the relation

$$\frac{L(t)}{\int_0^t L(t')t'dt'} = \frac{Q_{\text{dep}}(t)}{\int_0^t Q_{\text{dep}}(t')t'dt'}, \quad (9)$$

holds (Kushnir et al. 2013). Using Equations (7,9), Wygoda et al. (2019a) performed a one parameter fit to find t_0 values that best match the late-time light curve (*the integral method*) of well observed Type Ia SNe. This method requires the measurements of the bolometric luminosity from early times until $t \sim \text{few} \times t_0$ (although early times are less significant because the integral is time weighted). The fit, however, is ensured to maintain energy conservation. The value of t_0 can be used to find $M_{\text{Ni}56}$ by comparing the late-time light curve to the deposited energy given by Equations (3-5) with an estimated distance to the SN. Wygoda et al. (2019a) assumed the interpolating function of Equation (7) and found a tight range of γ -ray escape times, $t_0 \approx 35 - 40$ d, over the entire range of observed $M_{\text{Ni}56}$. These findings were used to constrain different Type Ia models. Note that Childress et al. (2015) found a much larger range of $t_0 \approx 13 - 48$ d, and specifically a very low value of $t_0 \approx 16$ d for SN 2011fe. As we show in Section 4, their value of t_0 for SN 2011fe is clearly inconsistent with the observations, and we also suggest there what was the source for this discrepancy.

Shussman et al. (2016) and Nakar et al. (2016) used

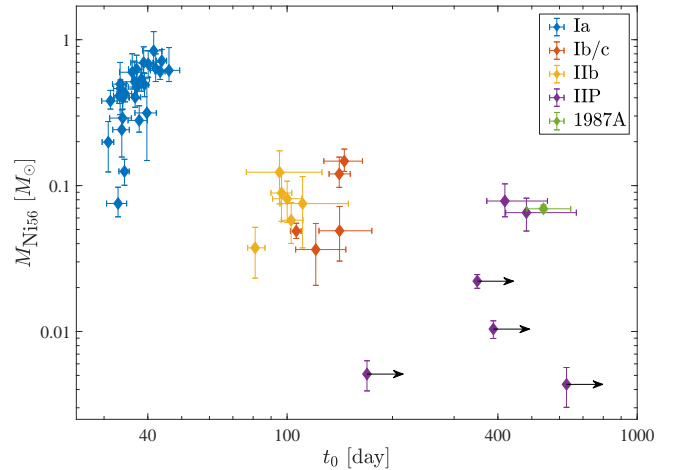


Figure 1. $M_{\text{Ni}56} - t_0$ distribution of the SNe sample. Different types of SNe, marked by different colours, are clustered around distinct typical t_0 values, while the synthesized ^{56}Ni amount overlaps among the different types. The tight range of γ -ray escape times, $t_0 \approx 30 - 45$ d, of Type Ia SNe (blue) is recovered, and we find a new tight range, $t_0 \approx 80 - 140$ d, for SE SNe (red: Type Ib/c, orange: Type IIb). Type IIP SNe (purple, SN 1987A in green) are clearly separated from other SNe types with $t_0 \gtrsim 400$ d, and there is a possible negative correlation between t_0 and $M_{\text{Ni}56}$. The error-bars correspond to 68 per cent confidence level around the median values (see the text for details).

Equation (8) to study Type IIP SNe, where the term $tE(t)$ cannot be neglected at early times. In this case, Equation (8) can be written (for times where $tE(t)$ is small) as

$$\int_0^t Q_{\text{dep}}(t')t'dt' = \int_0^t L(t')t'dt' - ET, \quad (10)$$

where ET is the integrated time-weighted luminosity that would be emitted if no ^{56}Ni was produced. The procedure was to find $M_{\text{Ni}56}$ from the nickel tail (assuming full deposition), and to derive ET from Equation (10). They found ET values of $\sim 10^{55}$ ergs, which is a substantial fraction of the total time-weighted luminosity.

Bolometric light curves of SE SNe have been constructed and studied in the past (e.g., Lyman et al. 2013; Wheeler et al. 2015; Lyman et al. 2016; Prentice et al. 2018b; Meza & Anderson 2020). The values of t_0 were estimated with two different methods by Wheeler et al. (2015). They either used Arnett’s rule with some extensions, or a fit to the late-time light curve, by using the exponential interpolating function, Equation (7), assuming positrons are not fully trapped (which is unrealistic, see Kushnir & Waxman 2020). Using the first method, they found $t_0 \approx 50 - 90$ d, while the second method yielded $t_0 \approx 100 - 300$ d (with some exceptions).

In this paper, we expand the use of the Katz integral to study the γ -ray deposition history of core-collapse SNe. The construction of bolometric light curves for a sample of SNe is described in Section 2. We find that throughout most of the available measurements, the ejecta is not sufficiently optically thin for the approximation of Equation (6) to hold. As a result, the interpolating function has a significant effect on the results, which forces us to introduce an additional ‘smoothness’ parameter, n , to the interpolating function of Equation (7). We therefore fit in Section 3 for four ejecta parameters: t_0 , n , $M_{\text{Ni}56}$ and ET . We use a sample of Type Ia SNe as a control sample, and we are able to recover the results of Wygoda et al. (2019a) with our method. The use of the additional parameter n allows us to reduce a ~ 10 per cent

systematic error that was introduced by the interpolation function of Equation (7) to the t_0 values of Type Ia SNe.

Our results are presented in Section 4. The main result is presented in Figure 1, where the distribution of t_0 as a function of $M_{\text{Ni}56}$ for various types of SNe is shown. As can be seen in the figure, we recover the tight range of γ -ray escape times, $t_0 \approx 30 - 45$ d, for Type Ia SNe, and we find a new tight range, $t_0 \approx 80 - 140$ d, for SE SNe. Type IIP SNe are clearly separated from other SNe types with $t_0 \gtrsim 400$ d, and there is a possible negative correlation between t_0 and $M_{\text{Ni}56}$.

Kushnir (2015b) used a compilation from the literature to show that the typical $M_{\text{Ni}56}$ in SE SNe are larger than those in Type IIP SNe¹. As can be seen in Figure 1, the result of Kushnir (2015b) still holds for our (smaller) sample, where the $M_{\text{Ni}56}$ are determined in a consistent way with systematic uncertainties under control. Meza & Anderson (2020) also reached the same conclusion, but their methods suffers from systematic effects that are hard to quantify (see discussion in Section 4). The larger typical values of $M_{\text{Ni}56}$ in SE SNe, as compared to $M_{\text{Ni}56}$ in Type IIP SNe, disfavours progenitors with the same initial mass range for these explosions (see detailed discussion in Kushnir 2015b).

In section 5, we apply a simple γ -ray radiation transfer code to calculate the γ -ray deposition histories of models from the literature, and we show that the observed histories are a powerful tool to constrain models. We discuss our results and conclude in Section 6.

2 BOLOMETRIC LIGHT CURVES SAMPLE

Our analysis requires the acquisition of bolometric light curves for several types of well-observed SNe. These were constructed using published photometry and estimated reddening values and distances (except for SN 1987A, for which we used the bolometric light curve of Suntzeff & Bouchet 1990). The SN sample is described in Section 2.1, and the bolometric light curve construction method is described in Section 2.2.

2.1 SNe sample

Our sample of well-observed SNe is composed of 27 Type Ia SNe, 11 SE SNe (5 Type Ib/c, 6 Type Iib), 7 Type IIP SNe and SN 1987A.

- **Type Ia SNe** –Photometry was taken from the Open Supernova Catalogue (Guillochon et al. 2017), the CSP data release 3 (Krisciunas et al. 2017; Burns et al. 2018), the Berkeley supernova Ia program (Silverman et al. 2012), the Lick Observatory Supernova Search Follow-up Photometry Program (Ganeshalingam et al. 2010), the Sternberg Astronomical Institute Supernova Light Curve Catalogue (Tsvetkov et al. 2004), the Harvard-Smithsonian Center for Astrophysics (CfA) (Hicken et al. 2009; Friedman et al. 2015), and the Swift Optical/Ultraviolet Supernova Archive (Brown et al. 2014). Additional photometry was taken from the individual SN studies of SN 2003du (Stanishev et al. 2007), SN 2004eo (Pastorello et al. 2007b), SN 2005cf (Pastorello et al. 2007a), SN 2011fe (Matheson et al. 2012; Mumari et al. 2013; Tsvetkov et al. 2013; Firth et al. 2015; Graham et al. 2017), SN 2012fr (Zhang et al. 2014; Contreras et al. 2018), and SN 2013dy (Pan et al. 2015; Zhai et al. 2016).

¹ This result was later reproduced by Anderson (2019), using similar methods.

- **SE SNe** –The sample consists of three SNe from the CSP-I SE sample photometry (Stritzinger et al. 2018a) with the distance and reddening estimation taken from (Taddia et al. 2018; Stritzinger et al. 2018b), SN 1993J (Richmond et al. 1996; Matthews et al. 2002)², SN 2002ap (Yoshii et al. 2003; Tomita et al. 2006), SN 2007gr (Hunter et al. 2009; Chen et al. 2014), SN 2008ax (Pastorello et al. 2008; Taubenberger et al. 2011; Bianco et al. 2014), SN 2009jf (Valenti et al. 2011), SN 2010as (Folatelli et al. 2014), SN 2011dh (Ergan et al. 2015)³, SN 2016coi (Prentice et al. 2018a; Ter-
reran et al. 2019).

- **Type IIP SNe** –The sample consists of SN 2004et (Sahu et al. 2006; Maguire et al. 2010), SN 2005cs (Pastorello et al. 2009), SN 2009N (Takáts et al. 2013), SN 2009md (Fraser et al. 2011), SN 2012A (Tomasella et al. 2013), SN 2013ej (Yuan et al. 2016)⁴, and SN 2017eaw (Rho et al. 2018; Szalai et al. 2019). Note that SN 2004et and SN 2017eaw occurred at the same host galaxy, so the distance estimate for both SNe was taken from Szalai et al. (2019).

- **SN 1987A** –The bolometric light curve was taken from Suntzeff & Bouchet (1990).

2.2 Constructing bolometric light curves

In this section, we describe the method we use to construct bolometric light curves from the photometric data. Our sample only includes SNe with photometry that covers the near-UV (U or u' band), optical, and near-infrared (IR) wavelengths for some phases of the SN. We require IR observations, since a significant fraction of the total flux of SE SNe is emitted in the IR wavelengths (Lyman et al. 2013; Prentice et al. 2016), reaching up to ~ 40 per cent at some phases. We find a similar IR fraction for our Type IIP sample, and a slightly lower fraction, ~ 30 per cent, for Type Ia SNe at some phases. The IR fraction has some non-trivial time evolution, and omitting the IR contribution changes our results significantly. Near UV measurements from *Swift* UVOT were also available sometimes. However, we have omitted data from the uvw1 and uvw2 bands, as they were inconsistent with the flux observed at neighbouring filters (see Figure 2). The motivation for this omission is the red leak (see Brown et al. 2016, for details). We have also omitted the data from the uvm2 band for phases later than 30 d since the explosion, because the UV contribution in these phases is quite small.

The bolometric light curve construction procedure begins with identification of missing data. For each considered band, we find all pairs of adjacent measurements with a magnitude difference larger than 0.5 magnitude and a time difference larger than 15 d. The missing data between each pair is estimated by using an adjacent auxiliary band, provided it has more complete data during these times. This is done by calculating the color between the two bands at the beginning and at the end of the considered time range, and linearly interpolating the color at the intermediate phases. This procedure is important in cases where the light curve changes fast, for example, at the transition from the plateau to the nickel tail of Type IIP SNe.

We next extrapolate for bands that lack observations at the beginning and at the end the light curve. This is done by

² Since photometric errors are not given, we estimate 0.1 mag error for all measurements.

³ Data up to 150 days from the explosion was used, see Appendix A for details.

⁴ This SN is generally regarded as Type IIL, but we do not make this distinction here.

assuming a constant color over the band with the missing data and the nearest band with data over the relevant time. This method introduces large uncertainties and should be done carefully, but since IR measurements do not always cover the time range of the optical measurements, extrapolating their magnitudes is preferable over omitting them. The errors introduced by this method increase as the time from the last measurement increases.

The light curves are then corrected for extinction using the methods of [Fitzpatrick \(1999\)](#), with the reddening values taken from the literature. The extinction-corrected light curves are then converted to flux densities at the effective wavelength of each band, creating a spectral energy distribution (SED) for each phase. The flux densities between the filters are linearly interpolated. To account for the missing UV contribution to the SED, we linearly extrapolate to zero flux at 2000 Å. The flux density for wavelengths longer than the longest effective wavelength band are estimated with a blackbody (BB) fit, calculated using the flux densities of bands with an effective wavelength higher than 5000 Å. Since all SNe in our sample contain IR measurements, the BB Rayleigh Jeans tail does not contribute more than a few per cents to the total flux (see also Figure 2). We do not consider epochs with three or less measured bands (without extrapolation). For example, if following some epoch, only the *B*, *V* and *R* bands were measured (and the rest of the bands were extrapolated), then these late epochs will not be included in the bolometric light curve. The obtained SED for a few phases of the Type Ic SN 2016coi are presented in Figure 2. The flux densities of the measured bands are marked with filled circles (black edges indicate interpolated values from an auxiliary band), and extrapolated values are marked with open circles. The large flux excess of the uvw1 and uvw2 bands, and the small contribution of the BB tail, are seen in the figure.

Finally, the total flux is calculated by trapezoidal integration of the SED and is converted to the luminosity using the luminosity distance. We also correct the time to the source frame, although this is a small correction for the low redshifts of our SNe sample ($z < 0.03$ for almost all SNe).

The uncertainty of the bolometric luminosity includes the given observed photometry (statistical) errors, which are propagated in the standard manner, and several sources of systematic errors. The systematic error includes the error due to the UV extrapolation, which we estimate by fixing zero flux at ± 500 Å away from the default 2000 Å, and the error of the BB extrapolation, which we estimate to be 25 per cent of the flux obtained in the BB regime. An additional 5 per cent of the total luminosity is added (as quadrature to the total error budget), accounting for additional unknown systematic errors. We (conservatively) treat this systematic error estimate as one standard deviation that is added to the (photometry) statistical uncertainty. As a result of this conservative error estimate, the total error is dominated by the significant systematic error uncertainty (see Figure 5), and statistical estimates for the model goodness-of-fit are not very informative (e.g. the χ^2 of the best-fitting models is significantly smaller than the number of degrees of freedom). Nevertheless, the uncertainty of the model parameters reflects the assumed systematic errors, and provides reliable estimate for possible models that can describe the observations. As we show in the following sections, this procedure allows us to draw strong conclusions, despite the large systematic errors. The treatment of the distance and extinction uncertainties is described in the next section.

Files containing the observed magnitudes, the processed magnitudes (after interpolation, extrapolation and de-

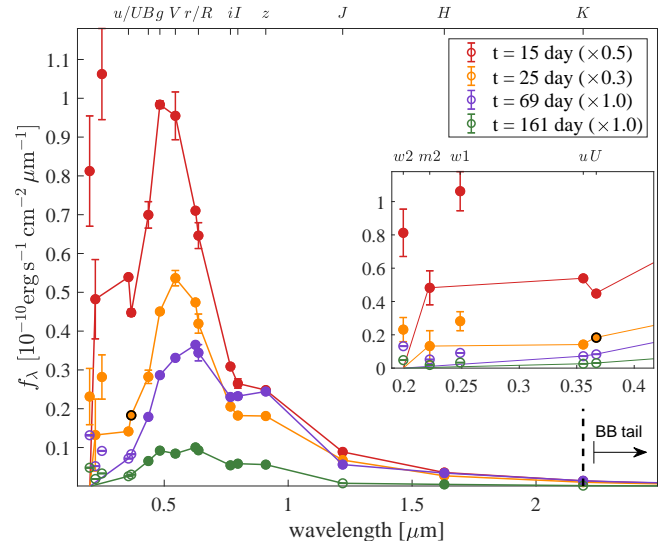


Figure 2. The obtained SED of SN 2016coi at several phases after explosion. The filled circles indicate the de-reddened flux intensity at the effective wavelength of each band, and the open circles correspond to the extrapolated values of the UV filters and the *J* and *K* bands at late times. The filled circles with black edges mark values interpolated with an auxiliary band. The solid lines represent the flux that is integrated for the calculation of the luminosity at each epoch. For clarity, the SED at $t = 15(25)$ d is scaled by 0.5(0.3). A magnification of the UV region shows the large flux excess of the *Swift* uvw1 and uvw2 filters, which are not taken into account for the construction of the SED. The BB region of the SED, covering wavelengths higher than the *K* band, is indicated with a dashed black line, and includes a small fraction of the SED at all epochs.

reddening), and the bolometric luminosity are included in the supplementary materials. The processed magnitudes file also contains the extinction coefficients, the distance and the explosion epoch that we use.

3 DEDUCING FOUR EJECTA PROPERTIES FROM THE BOLOMETRIC LIGHT CURVE

In this section, we expand the methods of [Wygoda et al. \(2019a\)](#) and [Nakar et al. \(2016\)](#) to extract various ejecta properties from the bolometric light curves. The case of SE SNe is more challenging to treat than the Type Ia SNe case for a number of reasons. The first is that ET , while not being as significant as in Type IIP SNe, is found to be non-negligible for most Type Ib/c SNe and for some Type IIb SNe. In order to include this parameter in our analysis, we use Equation (10) to write for times where $L = Q_{\text{dep}}$:

$$\frac{L(t)}{LT(t)} = \frac{\tilde{Q}_{\text{dep}}(t)}{\tilde{Q}T(t) + \tilde{E}T}, \quad (11)$$

where

$$LT(t) \equiv \int_0^t L(t')t' dt', \quad QT(t) \equiv \int_0^t Q_{\text{dep}}(t')t' dt', \quad (12)$$

and tilde stands for ^{56}Ni normalized quantities (for example, $\tilde{E}T = ET/M_{\text{Ni}56}$). The second difficulty is that in most of the available measurements of SE SNe, the ejecta is not sufficiently optically thin to γ -rays for the approximation of Equation (6) to hold. As a result, the shape of the interpolating function has a significant effect on the derived ejecta properties, forcing us to use a more versatile γ -ray deposition

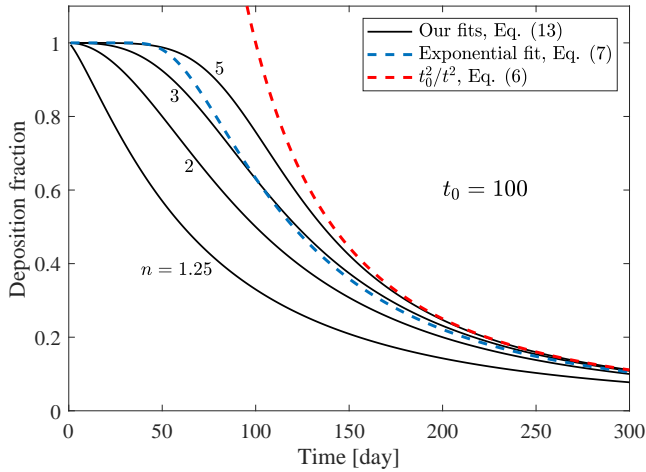


Figure 3. Deposition fraction as a function of time for $t_0 = 100$ d. The black solid lines represent the functions used in this analysis, Equation (13), for $n = 1.25, 2, 3, 5$ (bottom to top). The exponential function, Equation (7), is shown in the blue dashed line, and the late time behavior, Equation (6) is shown in the red dashed line. The parameter n controls the sharpness of the transition between optically thin and thick regimes. The larger n is, the sharper the transition is, and in the limit $n \rightarrow \infty$ the deposition fraction turns from being unity to following the behavior of Equation (6) at $t = t_0$.

function than Equation (7), which we found to be inappropriate both from fitting the data and from γ -ray transfer Monte Carlo simulations (see Section 5). We therefore introduce an additional parameter n to the interpolating function and replaced it with:

$$f_{\text{dep}}(t) = \frac{1}{(1 + (t/t_0)^n)^{\frac{2}{n}}}. \quad (13)$$

The parameter n controls the sharpness of the transition between optically thin and thick regimes. The larger n is, the sharper the transition is, and in the limit $n \rightarrow \infty$, the deposition fraction changes instantaneously from being unity to following the behavior of Equation (6) at $t = t_0$. Deposition functions for a few values of n and for a typical $t_0 = 100$ d value of SE SNe are shown in Figure 3, along with the exponential interpolating function, Equation (7). As can be seen in the figure, there is a large effect on the shape of the interpolating function up to $t \lesssim 200$ d (where most of the observed data is given). In addition, the effect of the interpolating function is enhanced, since deviations accumulate in the integrated luminosity LT .

The integral method is a three-parameter fit to Equation (11), in which we find the values of the triplet $\{t_0, \overline{ET}, n\}$ that minimize the expression

$$\frac{N_{\text{bins}}}{N_{\text{obs}}} \sum_{t_i \in t_{L=Q}} \left[\left(\frac{L(t_i)}{LT(t_i)} - \frac{\tilde{Q}_{\text{dep}}(t_i)}{\overline{QT} + \overline{ET}} \right) \frac{LT(t_i)}{L_{\text{err}}(t_i)} \right]^2. \quad (14)$$

The time range $t_{L=Q}$ accounts for the times where the assumption $L = Q_{\text{dep}}$ is valid (see below). The second factor in the squared parentheses accounts for the measurements errors of the ratio L/LT , assumed to be Gaussian, where we have neglected the error in LT . This is because LT is the sum of N_i independent measurements until t_i (with time weighting), so it is roughly suppressed by a factor $\sqrt{N_i}$. The $N_{\text{bins}}/N_{\text{obs}}$ factor is relevant for the estimation of the parameters uncertainty, which is discussed below, and does not affect the best-fitting values. This three-parameter fit is equivalent to maximizing the likelihood of the triplet $\{t_0, \overline{ET}, n\}$ to satisfy Equation (11), given the measurements errors. Note

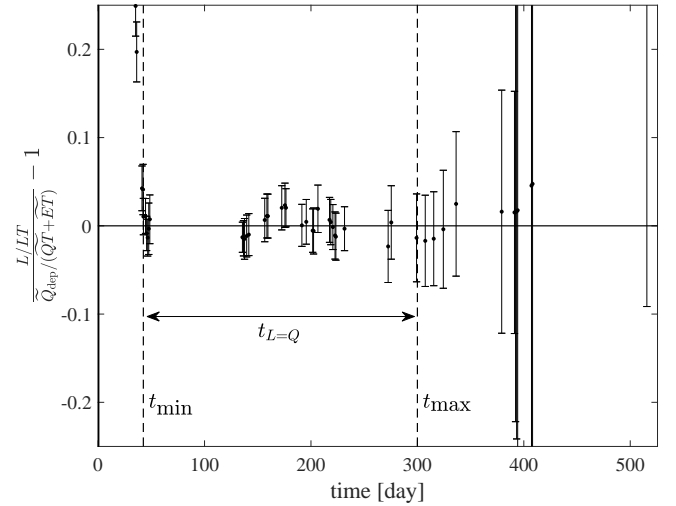


Figure 4. Relative error of the fit for SN 2002ap as a function of phase, with the error-bars being the statistical errors (the total errors are not presented for clarity). The vertical lines indicate the time range $t_{\min} = 42.5 \text{ d} \leq t_{L=Q} \leq t_{\max} = 300 \text{ d}$, over which the fit is being performed. The relative errors are distributed around zero during the calibrated $t_{L=Q}$ (this remains true until ~ 400 d). As a result, increasing t_{\min} would not change significantly the best-fitting parameters, and the relative errors during the original $t_{L=Q}$ would still be distributed around zero.

that this procedure is independent of $M_{\text{Ni}56}$ and of the distance to the SN. $M_{\text{Ni}56}$ is found by comparing the luminosity in the fitted range to the deposited radioactive energy.

We determine the time range $t_{\min} \leq t_{L=Q} \leq t_{\max}$, by fixing t_{\max} for each SN type and by determining t_{\min} self-consistently for each SN. A good choice for t_{\max} is $t_{\max} \sim \text{few} \times t_0$, since it allows us to determine t_0 with a reasonable accuracy, while observations at later time are usually at lower quality and includes a significant contribution from positrons (recall that following $t_c \approx 5t_0$ the energy deposition is dominated by positrons, such that it is more difficult to extract t_0). We fix $t_{\max} = 120$ d for Type Ia SNe, which is also roughly the median value of the last observational phase of our sample, and $t_{\max} = 300$ d for SE SNe. The available observations of Type IIP SNe force us to use $t_{\max} \sim 500$ d (ideally we would like to use $t_{\max} \sim 1500$ d), with slight variations for SN 2017eaw and 1987A. In cases that the phase of the last available data is smaller than t_{\max} , we fit until the last available phase. For most Type Ia and SE SNe that have measurements beyond t_{\max} , our fits provide good matches for $t > t_{\max}$, in some cases until the last available observation (see Appendix B). The value of t_{\min} is harder to determine, since the data does not provide a clear indication for the times in which the assumption $L = Q_{\text{dep}}$ is valid. Specifically, too small value for t_{\min} , with phases in which the assumption $L = Q_{\text{dep}}$ is not valid, would significantly bias the obtained fit parameters. In order to find self-consistently t_{\min} , we inspect the relative error of the fit, given by the deviation of $(L/LT)/(\tilde{Q}_{\text{dep}}/(\overline{QT} + \overline{ET}))$ from unity, during $t_{L=Q}$. For a self-consistently t_{\min} , the relative errors should be distributed around zero during $t_{L=Q}$. In this case, increasing t_{\min} would not change the best-fitting parameters significantly, and the relative errors during the original $t_{L=Q}$ would still be distributed around zero. We demonstrate this procedure in Figure 4, where the relative errors of the SN 2002ap fit are shown. The time range $t_{L=Q}$ of each SN is given in the bolometric luminosity file of the supplementary material.

An alternative method (the direct method) for deriv-

ing the four parameters, is to directly compare $L(t)$ during $t \in t_{L=Q}$ to the radioactive energy deposition rate. This method uses only the instantaneous luminosity, so ET is not a part of the calculation, but it requires $M_{\text{Ni}56}$, such that the number of parameters remains three: t_0 , n , and $M_{\text{Ni}56}$. ET can be calculated by taking the difference $LT - QT$ at late times. As explained in Section 1, for this method, observations with $t \gtrsim t_c$ are required in order to remove the degeneracy between $M_{\text{Ni}56}$ and t_0 ⁵. We find that, particularly for Type Ia SNe, the direct method is less stable than the integral method since it is more sensitive to the estimated time of explosion and to the values of t_{min} and t_{max} . It also has the disadvantage that the fit may result in a negative ET , which is not physical. However, it is still useful to apply both methods for validation and cross-checking. For most of the SNe in our sample, the variations of $M_{\text{Ni}56}$ and t_0 between the two methods are smaller than 10 per cent. For several Type Ia SNe, because of the degeneracy between t_0 and $M_{\text{Ni}56}$, the direct method finds considerably lower t_0 values than the integral method with large negative values of ET . We conclude that the values obtained by the integral method are more reliable.

Another advantage of the integral method for the analysis of Type Ia SNe, is that the ET parameter can be set to zero (as was done in [Wygoda et al. 2019a](#)), as expected for a white dwarf progenitor. To justify this simplification, we compare the results for Type Ia SNe with ET as a free positive parameter and without it. The results for most SNe remain the same, where the calibrated ET is negligibly small. For a few SNe, the t_0 values change by up to 7 per cent and gain an ET value of up to 3.5 per cent of the total time-weighted luminosity LT at infinity. This exercise allows us to identify suspicious light curves, where more detailed inspection is required.

The missing bolometric luminosity from explosion until the first observed epoch, have to be estimated for the calculation of LT . [Wygoda et al. \(2019a\)](#) suggested to interpolate linearly between the first epoch and $L = 0$ at $t = 0$. Since some Type Ia and SE SNe in our sample lack observation from very early times, we use instead a template of SN 2011fe (observed from hours since explosion) that is scaled to the first observed epoch. We found that the difference of the inferred parameters between the two methods is negligible. For Type IIP SNe, we assumed that the luminosity is constant from $t = 0$ up to the first epoch, and equals to the luminosity of the first epoch. Not extending the bolometric luminosity to $t = 0$ usually has a negligible effect, except for a few Type Ia SNe with relatively late first epoch measurements, and for a small influence on the ET value of core-collapse SNe.

The best-fitting results obtained with the integral method are demonstrated in Figure 5 for SN 2008aq (Type Iib), SN 2004et (Type IIP), and SN 1987A (Type II-pec). The entire sample is presented in Appendix B. The observed bolometric light curves are compared to the best-fitting models (solid lines) and to the radioactive energy generation rates (same as assuming $f_{\text{dep}} = 1$, dashed lines) in the left-hand side panels. In the right-hand side panels, the deposition functions f_{dep} that correspond to the best-fitting models (solid lines) are compared to the ratio $(L - Q_{\text{pos}})/Q_{\gamma}$. This ratio corresponds to L_{γ}/Q_{γ} for $t \in t_{L=Q}$, where we use the observed L and the derived Q_{pos} and Q_{γ} . The vertical dashed-dotted lines indicate the time range $t_{L=Q}$. As can be seen in the figure, the ejecta is not at the optically thin regime

⁵ The transition between the γ -ray optically thick and thin regimes also breaks this degeneracy. However, one has to trust that the interpolating function accurately describes the deposition during this transition.

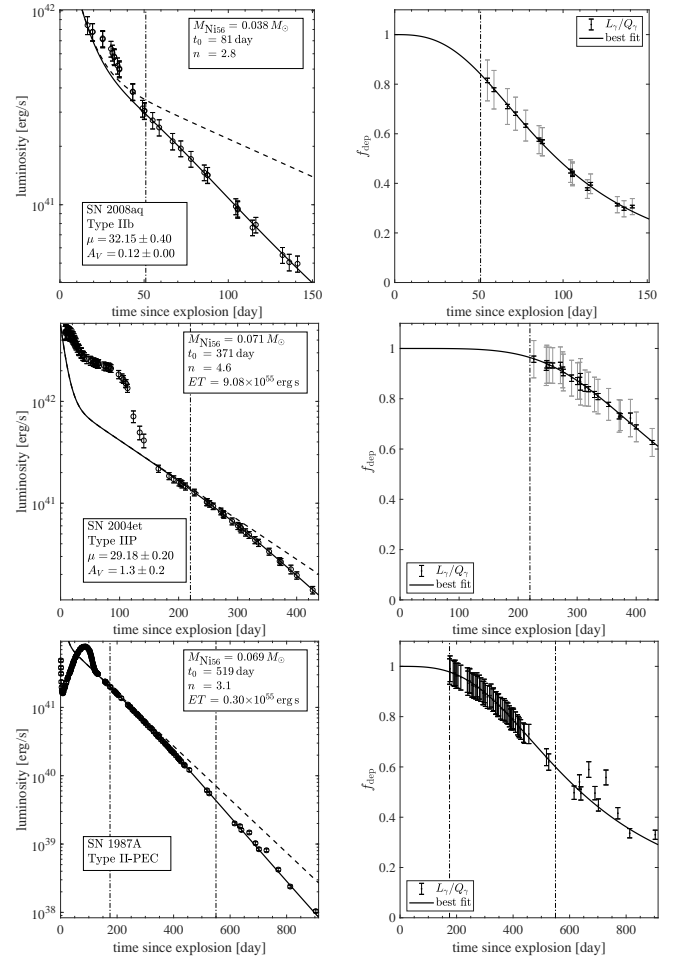


Figure 5. The best-fitting results of the integral method are demonstrated for SN 2008aq (Type Iib), SN 2004et (Type IIP), and SN 1987A (Type II-pec). The rest of the SNe in our sample are presented in Appendix B. The median values and 68% confidence level of the parameters are presented in Table 1. left-hand side panels: the observed bolometric light curves are compared to the best-fitting models (with the parameters given in the boxes, solid lines) and to the radioactive energy generation rates (same as assuming $f_{\text{dep}} = 1$, dashed lines). The distance and extinction estimates are given in the boxes as well. The errors represent the total errors (statistical and systematic). The bolometric light curve of SN 1987A was taken from the literature, so the errors (not shown) were set to 5% of the total luminosity, and the distance and extinction were not used. right-hand side panels: The deposition functions, f_{dep} , that correspond to the best-fitting models (solid lines) are compared to the ratio $(L - Q_{\text{pos}})/Q_{\gamma}$. This ratio corresponds to L_{γ}/Q_{γ} for $t \in t_{L=Q}$, where we use the observed L and the derived Q_{pos} , Q_{γ} . The total errors (statistical and systematic) are indicated by grey bars, while the (photometric) statistical errors are indicated by black bars. The treatment of the large systematic errors is discussed in the text. In both panels, the epochs of t_{min} and t_{max} (if different from the last phase) are indicated by vertical dashed-dotted lines.

for almost the entire time-span of the observations, and the shape of the interpolating function has a large effect. Additionally, for both SN 2004et (Type IIP) and SN 1987A, the γ -rays are not fully trapped at late times.

As discussed in Section 2, the total error is dominated by the significant systematic error uncertainty, and statistical estimates for the model goodness-of-fit are not very informative (e.g. the χ^2 of the best-fitting models is significantly smaller than the number of degrees of freedom). We estimate in the following section the uncertainty of the model param-

eters, which will reflect the assumed systematic errors. This estimate provides reliable estimate for possible models that can describe the observations.

3.1 The uncertainty of the parameters

The uncertainty of the observed bolometric light curve introduces errors to the fitted parameters. We estimate the median and the 68 per cent confidence levels by performing a Markov Chain Monte Carlo (MCMC) algorithm using the MCMCSTAT MATLAB package⁶, where the likelihood function is Equation (14) and the priors are uniformly distributed over reasonable domains. The priors for t_0 and \widetilde{ET} are $[0, \infty)$. The prior for n is $[1, 5)$, since below $n = 1$ the derivative of Equation (13) diverges at $t \rightarrow 0$ and creating a profile with $n \geq 5$ using our γ -ray transfer Monte Carlo code required extremely centred ^{56}Ni distribution (and for all SNe in our sample we find $n < 5$).

The $N_{\text{bins}}/N_{\text{obs}}$ factor in the likelihood function, Equation (14), represents the ratio between the number of independent time bins, N_{bins} , to the number of observations, N_{obs} , and is always ≤ 1 . We introduce this factor since the uncertainty is dominated by systematic errors, such that one cannot assume that the observations are statistically independent. Instead, since the typical systematic error is ~ 10 per cent, we estimate N_{bins} as the number of times that Q_{dep} changes by 10 per cent over the time range of each SN. For Type Ia SNe, with the longest duration of $40 \text{ d} \leq t_{L=Q} \leq 120 \text{ d}$ and typical t_0 values, we find at most $N_{\text{bins,max}} \approx 24$, such that the average duration of each independent bin is $\approx 3.5 \text{ d}$. For SE SNe, with the longest duration of $50 \text{ d} \leq t_{L=Q} \leq 300 \text{ d}$, we find at most $N_{\text{bins,max}} \approx 40$, and for Type IIP, with the longest duration of $130 \text{ d} \leq t_{L=Q} \leq 500 \text{ d}$, we find $N_{\text{bins,max}} \approx 43$. We determine N_{bins} for each SN as the ceiling of the maximal number of bins of that type multiplied with the ratio of $t_{L=Q}$ to the maximal duration. For example, the time range of the Type Ib/c SN 2007gr is $87 \leq t_{L=Q} \leq 183$, so we find

$$N_{\text{bins}} = \left\lceil \frac{183 - 87}{300 - 50} \times 40 \right\rceil = 16. \quad (15)$$

As explained above, the values of the triplet $\{t_0, \widetilde{ET}, n\}$ are independent of the distance to the SN. However, the values of M_{Ni56} and ET depend on the distance to the SN, and as a result, we propagate the distance uncertainty to the errors of these parameters.

In order to estimate the effect of the uncertainty of the extinction, we construct two additional light curves for each SN by using the upper and lower 1σ uncertainty of the extinction. We find the four parameters for these light curves using the same procedure. The error due to extinction uncertainty is determined as half the difference between the obtained parameters of the high and low extinction light curves, and is propagated to the errors as well. The extinction uncertainty mainly affects the errors estimate of M_{Ni56} and ET , and can only lead to a few percent uncertainty for t_0 and n in the case of high extinction uncertainties ($\delta E(B-V) \gtrsim 0.1$). In two Type IIB SNe with low ET values (SN 1993J and SN 2008ax), the lower ET limits become negative after this process, so we fixed them to zero in order to remain consistent with our priors.

4 THE EJECTA PROPERTIES OF THE SNE SAMPLE

The bolometric light curve parameters, derived using the integral method, for the SNe sample, are given in Table 1. The values in Table 1 are the median values of the posterior distribution of the parameters, together with the 68 per cent confidence level (note that the values presented in Appendix B are the best-fitting values). Except for Type IIP SNe, the best-fitting and median t_0 values of most SNe agree to within 1 per cent, while some differ by up to ~ 5 per cent. The relative uncertainty of the n parameter is larger than the relative uncertainty of t_0 , since n is largely dependent on the deposition function at early times, typically not satisfying the condition $L = Q_{\text{dep}}$.

The main result is presented in Figure 1, where the distribution of t_0 as a function of M_{Ni56} for various types of SNe is shown (plotted are the median values). As can be seen in the figure, we were able to recover the tight range of γ -ray escape time, $t_0 \approx 30 - 45 \text{ d}$, for Type Ia SNe (Wygoda et al. 2019a). The Type Ia SNe M_{Ni56} values range from $0.075 \pm 0.029 M_{\odot}$ for the faint SN 2007N to $\sim 0.8 M_{\odot}$, with an average value of $\approx 0.5 M_{\odot}$. Our t_0 values are within 10% of the results of Wygoda et al. (2019a), with the differences either due to the more careful construction of the bolometric light curve or due to the more versatile deposition interpolating function. We find a new tight range, $t_0 \approx 80 - 140 \text{ d}$, for SE SNe, with Type Ib/c having somewhat higher values than Type IIB ($107 - 140 \text{ d}$ for Type Ib/c and $80 - 110 \text{ d}$ for Type IIB). The average M_{Ni56} of SE SNe, $\approx 0.08 M_{\odot}$, is lower than the average value of Type Ia SNe, with almost the same values for Type Ib/c and Type IIB SNe. The t_0 values of Type IIP are much larger, and it is therefore much harder to evaluate their deposition functions. We are only able to determine the deposition function for three SNe (SN 2004et, SN 2017eaw and SN 1987A), while for the rest of the Type II SNe we can only able to provide a lower limit for t_0 (although M_{Ni56} and ET are measured to 20% accuracy, with the distance and extinction uncertainties being the main cause for the error). The lower limit was obtained by finding the t_0 value that would lead to a deposition equal to the mean value of the last three available phases, using the measured value of M_{Ni56} and $n = 5$ (which is higher than any value in the sample, with a lower n leading to a higher t_0). This lower limit is roughly the time of the last measurement. Type IIP SNe are clearly separated from other SNe types with $t_0 \gtrsim 400 \text{ d}$, and have a possible negative correlation between t_0 and M_{Ni56} . We find that the typical M_{Ni56} of SE SNe are larger than those of Type IIP SNe, in agreement with Kushnir (2015b).

The distribution of ET/LT_{200} , where $LT_{200} = LT(200 \text{ d})$, as a function of M_{Ni56} , is shown in Figure 6. We choose to compare at 200 d since usually luminosity observations are available at this time and the condition $L = Q_{\text{dep}}$ applies for almost all SNe. However, since a few SNe lack observations at this time, we approximate for all SNe, $LT_{200} \approx QT(200 \text{ d}) + ET$, using the best-fitting values, which introduces a small error. Note that the derivation of ET/LT_{200} is independent of M_{Ni56} and of the distance to the SN. As can be seen in the figure, the fraction ET/LT_{200} is between 0.45 to 0.75 for all Type IIP SNe, despite large variations in M_{Ni56} and overall luminosity. The derived ET values of SE SNe are smaller and more difficult to evaluate. We find for all Type Ib/c SNe in our sample ET/LT_{200} values of about 6 – 14 per cent. The ET/LT_{200} values of all Type IIB SNe are below ~ 6 per cent, and for SN 1987A we find an $ET/LT_{200} \sim 5$ per cent. As discussed above, Type Ia SNe do not have a detectable ET

⁶ <https://mjmlaine.github.io/mcmcstat/>

Table 1. The bolometric light-curve parameters, derived using the integral method. The values of the derived parameters are the median values of the posterior distribution, together with the 68 per cent confidence levels.

Type	Name	μ^a	$E(B-V)_{\text{MW}}^b$	$E(B-V)_{\text{host}}^c$	$R_V^{\text{host}, d}$	M_{Ni56} (M_{\odot})	t_0 (day)	ET (10^{55} ergs)	n
Ia	2003du	32.79 ± 0.04	0.01	0.00 ± 0.05	3.1	$0.60^{+0.20}_{-0.14}$	$36.1^{+2.1}_{-2.9}$	0	$3.0^{+1.3}_{-1.1}$
	2004eo	34.12 ± 0.10	0.11	0.00 ± 0.01	3.1	$0.47^{+0.14}_{-0.08}$	$37.3^{+1.8}_{-2.1}$	0	$2.6^{+1.3}_{-1.0}$
	2004gs	35.49 ± 0.05	0.03	0.19 ± 0.01	1.9	$0.40^{+0.09}_{-0.07}$	$33.9^{+1.5}_{-1.9}$	0	$2.0^{+0.7}_{-0.5}$
	2005cf	32.29 ± 0.10	0.10	0.09 ± 0.03	3.1	$0.63^{+0.15}_{-0.12}$	$37.2^{+1.7}_{-1.9}$	0	$2.7^{+1.2}_{-0.8}$
	2005el	34.04 ± 0.40	0.10	0.01 ± 0.01	3.1	$0.50^{+0.20}_{-0.19}$	$33.3^{+1.4}_{-1.6}$	0	$3.3^{+1.1}_{-1.0}$
	2005eq	35.40 ± 0.04	0.06	0.11 ± 0.02	2.4	$0.84^{+0.30}_{-0.18}$	$41.6^{+2.3}_{-2.9}$	0	$1.9^{+1.1}_{-0.6}$
	2005ke	31.86 ± 0.19	0.02	0.32 ± 0.03	1	$0.13^{+0.03}_{-0.02}$	$34.3^{+1.1}_{-1.2}$	0	$3.3^{+0.8}_{-0.6}$
	2005ki	34.67 ± 0.05	0.03	0.02 ± 0.01	1.4	$0.46^{+0.07}_{-0.05}$	$33.4^{+1.2}_{-1.5}$	0	$3.2^{+0.9}_{-0.7}$
	2006D	32.97 ± 0.10	0.04	0.14 ± 0.01	1.6	$0.41^{+0.06}_{-0.05}$	$33.2^{+1.1}_{-1.2}$	0	$3.8^{+0.8}_{-0.8}$
	2006hb	34.08 ± 0.07	0.02	0.09 ± 0.02	1.8	$0.28^{+0.07}_{-0.05}$	$37.8^{+2.1}_{-2.7}$	0	$2.5^{+1.1}_{-0.7}$
	2006is	35.40 ± 0.06	0.03	0.01 ± 0.01	1.6	$0.62^{+0.27}_{-0.10}$	$46.0^{+3.3}_{-5.3}$	0	$2.8^{+1.4}_{-1.2}$
	2006kf	34.80 ± 0.05	0.21	0.04 ± 0.02	1.8	$0.38^{+0.07}_{-0.05}$	$31.3^{+1.4}_{-1.7}$	0	$3.4^{+1.1}_{-1.0}$
	2007N	33.93 ± 0.09	0.03	0.44 ± 0.04	1.3	$0.08^{+0.02}_{-0.01}$	$32.9^{+1.9}_{-2.4}$	0	$2.3^{+1.1}_{-0.7}$
	2007af	31.72 ± 0.07	0.01	0.13 ± 0.02	3.1	$0.40^{+0.07}_{-0.06}$	$36.8^{+1.4}_{-1.5}$	0	$2.9^{+1.0}_{-0.7}$
	2007as	34.44 ± 0.06	0.12	0.12 ± 0.03	1.4	$0.52^{+0.20}_{-0.09}$	$36.7^{+2.1}_{-2.9}$	0	$2.5^{+1.5}_{-1.0}$
	2007hj	33.94 ± 0.08	0.07	0.12 ± 0.02	1.4	$0.29^{+0.09}_{-0.05}$	$33.9^{+2.0}_{-2.8}$	0	$2.5^{+1.3}_{-0.8}$
	2007le	32.23 ± 0.16	0.03	0.38 ± 0.02	1.9	$0.64^{+0.16}_{-0.12}$	$42.1^{+1.6}_{-1.6}$	0	$2.9^{+1.3}_{-1.0}$
	2007on	31.28 ± 0.36	0.01	0.00 ± 0.05	3.1	$0.20^{+0.08}_{-0.07}$	$30.8^{+1.1}_{-1.2}$	0	$3.9^{+0.7}_{-0.8}$
	2008bc	34.15 ± 0.06	0.23	0.02 ± 0.02	1.5	$0.70^{+0.20}_{-0.10}$	$38.9^{+2.4}_{-3.2}$	0	$3.0^{+1.3}_{-1.1}$
	2008fp	31.72 ± 0.14	0.17	0.52 ± 0.03	2.2	$0.68^{+0.16}_{-0.13}$	$40.1^{+1.5}_{-1.7}$	0	$3.3^{+1.1}_{-1.0}$
	2008hv	33.76 ± 0.08	0.03	0.01 ± 0.01	1.1	$0.43^{+0.08}_{-0.05}$	$34.5^{+1.5}_{-1.8}$	0	$3.3^{+1.1}_{-0.9}$
	2009Y	33.13 ± 0.09	0.09	0.15 ± 0.03	1.3	$0.72^{+0.14}_{-0.11}$	$43.8^{+1.4}_{-1.5}$	0	$2.3^{+0.8}_{-0.5}$
	2011fe	29.03 ± 0.17	0.01	0.03 ± 0.01	3.1	$0.49^{+0.09}_{-0.09}$	$39.1^{+1.1}_{-1.2}$	0	$3.4^{+0.9}_{-0.8}$
	2012fr	31.27 ± 0.05	0.02	0.03 ± 0.01	3.1	$0.61^{+0.09}_{-0.07}$	$43.4^{+1.4}_{-1.5}$	0	$2.8^{+1.0}_{-0.7}$
	2012ht	31.50 ± 0.40	0.02	0.00 ± 0.01	3.1	$0.24^{+0.09}_{-0.08}$	$33.7^{+1.7}_{-2.0}$	0	$3.7^{+0.9}_{-1.0}$
	2013dy	30.68 ± 0.48	0.14	0.15 ± 0.06	3.1	$0.31^{+0.17}_{-0.17}$	$39.8^{+2.5}_{-3.0}$	0	$3.0^{+1.2}_{-0.9}$
	2015F	31.89 ± 0.04	0.18	0.04 ± 0.03	3.1	$0.54^{+0.15}_{-0.10}$	$38.4^{+2.1}_{-2.3}$	0	$3.0^{+1.2}_{-1.1}$
Ib/c	2002ap	29.50 ± 0.10	0.09	0.00 ± 0.01	3.1	$0.05^{+0.01}_{-0.01}$	106^{+4}_{-4}	$0.14^{+0.04}_{-0.04}$	$2.4^{+0.6}_{-0.5}$
	2007C	31.61 ± 0.40	0.04	0.55 ± 0.04	2.4	$0.04^{+0.02}_{-0.02}$	120^{+28}_{-15}	$0.25^{+0.12}_{-0.14}$	$2.6^{+1.5}_{-1.1}$
	2007gr	30.13 ± 0.35	0.06	0.03 ± 0.02	3.1	$0.05^{+0.02}_{-0.02}$	140^{+35}_{-17}	$0.41^{+0.18}_{-0.22}$	$2.4^{+1.5}_{-1.0}$
	2009jf	32.65 ± 0.10	0.11	0.05 ± 0.05	3.1	$0.15^{+0.03}_{-0.02}$	147^{+19}_{-19}	$0.81^{+0.44}_{-0.44}$	$3.3^{+1.1}_{-1.1}$
	2016coi	31.29 ± 0.16	0.08	0.13 ± 0.03	3.1	$0.12^{+0.04}_{-0.02}$	141^{+11}_{-9}	$0.97^{+0.39}_{-0.49}$	$2.8^{+1.3}_{-1.0}$
IIB	1993J	27.78 ± 0.18	0.07	0.10 ± 0.10	3.1	$0.08^{+0.03}_{-0.03}$	100^{+10}_{-9}	$0.23^{+0.18}_{-0.17}$	$3.0^{+0.8}_{-0.6}$
	2006T	32.50 ± 0.41	0.07	0.32 ± 0.04	1.3	$0.07^{+0.04}_{-0.04}$	109^{+29}_{-14}	$0.23^{+0.13}_{-0.13}$	$2.5^{+1.4}_{-1.0}$
	2008aq	32.15 ± 0.40	0.04	0.00 ± 0.00	0	$0.04^{+0.01}_{-0.01}$	81^{+6}_{-4}	$0.00^{+0.00}_{-0.00}$	$2.8^{+0.8}_{-0.6}$
	2008ax	29.91 ± 0.29	0.02	0.38 ± 0.10	3.1	$0.09^{+0.03}_{-0.03}$	96^{+7}_{-7}	$0.17^{+0.14}_{-0.14}$	$2.9^{+0.8}_{-0.6}$
	2010as	32.16 ± 0.36	0.15	0.42 ± 0.10	1.5	$0.12^{+0.05}_{-0.05}$	94^{+32}_{-18}	$0.00^{+0.00}_{-0.00}$	$1.7^{+1.1}_{-0.5}$
	2011dh	29.46 ± 0.28	0.03	0.04 ± 0.07	3.1	$0.06^{+0.02}_{-0.02}$	103^{+8}_{-7}	$0.14^{+0.10}_{-0.10}$	$3.4^{+1.0}_{-0.9}$
IIP	2004et	29.18 ± 0.20	0.34	0.07 ± 0.07	3.1	$0.078^{+0.026}_{-0.017}$	419^{+153}_{-48}	$8.66^{+2.26}_{-2.34}$	$2.8^{+1.5}_{-1.3}$
	2005cs	29.26 ± 0.33	0.03	0.02 ± 0.01	3.1	$0.004^{+0.001}_{-0.001}$	> 628	$1.05^{+0.32}_{-0.32}$	$3.0^{+1.3}_{-1.4}$
	2009N	31.67 ± 0.11	0.02	0.11 ± 0.02	3.1	$0.022^{+0.002}_{-0.002}$	> 349	$1.38^{+0.18}_{-0.18}$	-
	2009md	31.64 ± 0.21	0.03	0.07 ± 0.10	3.1	$0.005^{+0.001}_{-0.001}$	> 169	$0.65^{+0.20}_{-0.20}$	-
	2012A	29.96 ± 0.15	0.03	0.01 ± 0.01	3.1	$0.010^{+0.001}_{-0.001}$	> 388	$1.19^{+0.19}_{-0.19}$	-
	2013ej	29.93 ± 0.11	0.06	0.00 ± 0.01	3.1	$0.022^{+0.004}_{-0.003}$	> 338	$4.05^{+0.48}_{-0.47}$	-
	2017eaw	29.18 ± 0.20	0.30	0.11 ± 0.10	3.1	$0.066^{+0.017}_{-0.016}$	495^{+258}_{-71}	$5.93^{+1.83}_{-1.84}$	$2.9^{+1.3}_{-1.2}$
II-pec	1987A	18.56 ± 0.05	-	-	-	$0.069^{+0.004}_{-0.004}$	533^{+78}_{-51}	$0.28^{+0.13}_{-0.15}$	$2.9^{+0.8}_{-0.6}$

^a Distance modulus^b Galactic extinction towards the SN^c Host extinction^d Host $R_V = A_V/E(B-V)_{\text{host}}$ [†] For SN 1987A, the bolometric light curve was taken from the literature, so the extinction estimates are not used.

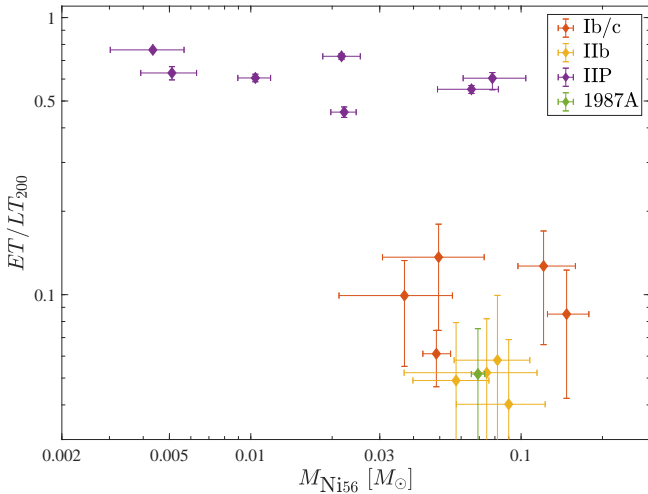


Figure 6. The fraction ET/LT_{200} as a function of M_{Ni56} . The values of ET/LT_{200} are similar for all Type IIP SNe (purple), despite large variations in M_{Ni56} and in the overall luminosity. The derived ET values of SE SNe (red and orange) and of SN 1987A (green) are smaller and more difficult to evaluate. We believe that our systematic errors are of the order of 10 per cent, so we treat the ET measurement for SE SNe as tentative.

value. We believe that our systematic errors are of the order of 10 per cent, so we treat the ET measurement for SE SNe as tentative.

We can further calculate ET by using the distances to the SNe. Figure 7 shows the $ET - t_0$ distribution of our sample. As can be seen in the figure, Type IIb SNe have ET values of up to $\approx 2.5 \times 10^{54}$ ergs, with two of the SNe having negligible values and are not shown. Type Ib/c SNe have larger values, ranging from $\approx 1.5 \times 10^{54}$ ergs to $\approx 10^{55}$ ergs. There is a possible positive correlation between ET and t_0 for SE SNe. We note again that we treat the ET measurement for SE SNe as tentative. Type IIP SNe have the largest ET values, from $\approx 6.5 \times 10^{54}$ ergs to $\approx 8.5 \times 10^{55}$ ergs. The derived ET values agree to within 20 per cent with the values given by Nakar et al. (2016). Inconsistencies are mainly due to differences between the adopted bolometric light curves. We find that Type IIP SNe with a measurable t_0 have larger ET values, but the sample is too small to draw strong conclusions.

4.1 Comparison to previous works

The derived M_{Ni56} for the Type Ia SNe and SE SNe sample are almost always lower than the values predicted by Arnett’s rule. For example, the M_{Ni56} derived for the CSP SNe in our sample are lower than the Arnett’s rule estimates of Taddia et al. (2018) for the same SNe by roughly 10 per cent (SN 2006T), 25 per cent (SN 2008aq) and 45 per cent (SN 2007C). Dessart et al. (2016) also reported an overestimate of Arnett’s rule for their models. This is probably due to the simplifying assumptions used in deriving Arnett’s rule. Meza & Anderson (2020) used pseudo bolometric light curves to estimate the M_{Ni56} of SE SN using Arnett’s rule. Their light curves were constructed from the B band to the H band, so their luminosity for the same SN was almost always lower than ours, typically by tens of per cents. This underestimate of the bolometric light curve compensated for the higher M_{Ni56} derived by Arnett’s rule, such that their derived M_{Ni56} are similar to our values, with our sample having slightly lower values on average. Meza & Anderson (2020) used the method of Khatami & Kasen (2019), which is a variant of the Katz integral that uses the peak time and includes

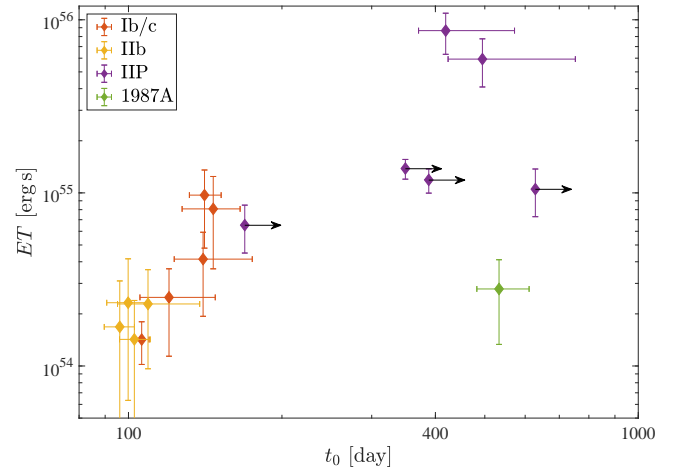


Figure 7. The $ET - t_0$ distribution of our sample. The derived ET values of Type IIP SNe agree to within 20 per cent with the values given by Nakar et al. (2016). SE SNe show a positive correlation between ET and t_0 , though we treat the ET measurement for SE SNe as tentative. Type IIP SNe with a measurable t_0 have larger ET values.

a free parameter that cannot be calibrated from the observations (see also Kushnir & Katz 2019). The uncertainty of using this method is substantial and hard to estimate. Finally, Meza & Anderson (2020) used the direct method, but with the assumption of full γ -ray deposition (that is unrealistic according to our results), which provides a poor description of the observations (tens of per cent discrepancy).

We further compare our results to those previously derived for Type Ia SNe by different methods. Scalzo et al. (2019) estimated M_{Ni56} and t_0 for their Type Ia SNe sample using hydrodynamic modelling, which includes various simplifying assumptions, and found, for the same SNe, values that are generally lower than ours. Using ^{56}Co emission lines in nebular phase spectra, Childress et al. (2015) derived t_c (related to t_0 by $t_0 \approx 0.18t_c$) for six Type Ia SNe. They found a span of 13.2 – 48.2 d in t_0 values, much larger than our results and from those of Wygoda et al. (2019a). Four of these SNe were also analysed by us. For SN 2003du, Childress et al. (2015) derived a value of 35.1 ± 4.1 d, consistent with our result of 35.8 ± 4.2 d. The value of SN 2012fr was somewhat lower than ours, 34.7 ± 4.0 d compared to 43.3 ± 0.9 d, respectively. For SN 2007af and SN 2011fe, the t_0 values derived by Childress et al. (2015) are 13.3 ± 3.8 d and 16.4 ± 2.1 d, which are much lower than our values of 36.7 ± 1.2 d and 39.4 ± 0.4 d, respectively. In Figure 8, we compare the light curve and the γ -ray deposition fraction of SN 2011fe to the best fit values of Childress et al. (2015). It is clear that the t_0 derived by Childress et al. (2015) is too low to explain the light curve evolution. We suggest that the reason for this discrepancy is their assumption that the ejecta is optically thin already at $t \sim 100$ d.

We find that the t_0 values we derived for the SE SNe sample are lower than the results of Wheeler et al. (2015), which were derived by fitting the late time light-curve luminosity to the radioactive energy deposition rate. In their analysis, they used the exponential interpolating deposition function, Equation (7), and incomplete positron trapping was assumed (which is not realistic, see Kushnir & Waxman 2020). Their values are ≈ 30 per cent (SN 1993J) to ≈ 140 per cent (SN 2009jf) higher than our values. We try to reproduce their results by using the same interpolating function and assuming incomplete positron trapping, and we find that t_0 increase by 5 – 10 per cent. This increment brings some t_0 values closer

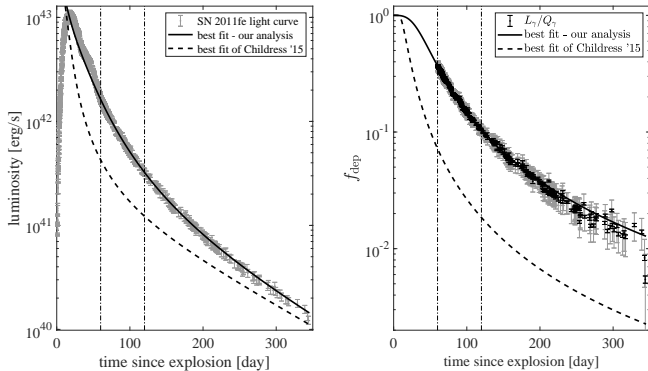


Figure 8. Same as 5 for SN 2011fe. left-hand side panel: The observed bolometric light curve (grey symbols), our best-fitting model (solid line) and best fit of [Childress et al. \(2015\)](#), dashed line) with the exponential interpolating function (Equation (7)). right-hand side panel: the γ -ray deposition fraction L_γ/Q_γ , and the deposition model of [Childress et al. \(2015\)](#), dashed line). It is clear that the $t_0 \approx 16$ d derived by [Childress et al. \(2015\)](#) is too low to explain the light curve evolution.

to the ones derived by [Wheeler et al. \(2015\)](#), like SN 1993J, but most SNe still differ by tens of per cents.

5 CONSTRAINING EJECTA PARAMETERS WITH γ -RAY TRANSFER SIMULATIONS

In this section, we demonstrate that the derived γ -ray deposition histories from Section 4 offer a powerful tool for constraining models. The application for Type Ia SNe was already discussed by [Wygoda et al. \(2019a\)](#), so we focus on SE SNe (Section 5.1) and on Type II SNe (Section 5.2). We apply a Monte Carlo (MC) γ -ray transfer simulations to models from the literature, which allows us to measure the values of t_0 and n (note that t_0 can be obtained directly from the models without performing transfer simulation, by averaging over the ^{56}Ni optical depth, see [Wygoda et al. 2019a](#)). The MC γ -ray transfer code is similar to the one described by [Wygoda et al. \(2019a,b\)](#). In Section 5.3 we compare the observed ET values of our core-collapse sample to the models predictions and we discuss the implications of this comparison. The model parameters and the results of the simulations are presented in Appendix C. The parameters consist of the ejecta mass, M_{ej} , the kinetic energy, the amount of ^{56}Ni mixing, and the ratio of ejecta mass to the square root of kinetic energy. The amount of ^{56}Ni mixing is defined as

$$\frac{\int X_{\text{Ni}56}(m)dm}{M_{\text{ej}}M_{\text{Ni}56}} \quad (16)$$

where $X_{\text{Ni}56}$ is the ^{56}Ni mass fraction and m is the enclosed mass. This is a measure of the ^{56}Ni normalized ‘centre of mass’. Profiles with centered ^{56}Ni distribution will have mixing values close to 0, whereas a fully and uniformly mixed distribution will have a mixing value of 0.5.

5.1 SE SNe comparison with models – n and t_0

The $n - t_0$ distribution of SE SNe with relatively a low t_0 error (three Type Ib/c, four Type IIb), is shown in Figure 9. Also shown are these parameters for several models from the literature (kindly provided to us by the authors of [Blinnikov et al. 1998](#); [Dessart et al. 2016](#); [Yoon et al. 2019](#)), calculated with the MC γ -ray transfer code.

[Yoon et al. \(2019\)](#) simulated Type Ib/c SN progenitors with different explosion energies and ^{56}Ni mixing. We examine two models, shown as green symbols in Figure 9. The first, HE3.87, simulated a Type Ib SN, with an ejecta mass of $M_{\text{ej}} = 2.4 M_\odot$, and the second, CO3.93, simulated a Type Ic SN, with an ejecta mass of $M_{\text{ej}} = 2.49 M_\odot$. Each model has several kinetic energy values and different levels of ^{56}Ni mixing. [Yoon et al. \(2019\)](#) compared the light curves and the early-time color evolutions of observed Type Ib/c SNe to the models. They found that models with moderate mixing, $f_m = 0.15 - 0.5$, agree well with Type Ib SNe, while Type Ic SNe are better described by models with high mixing, $f_m = 0.5 - 5$. We find that the values of t_0 are mainly determined by the kinetic energy (see discussion below) and, to some extent, by the amount of mixing. The values of n are almost solely determined by the level of mixing. As can be seen in the figure, profiles with low mixing, shown as triangles ($f_m = 0.15$, see [Yoon et al. 2019](#), for details) have large values of n and are in disagreement with our analysis, while profiles with moderate mixing ($f_m = 0.5$, shown as circles), or high mixing ($f_m = 5$, diamonds) have lower values of n and are in better agreement with our analysis. Models with relatively high kinetic energies ($E_{\text{kin}} > 1.5 \times 10^{51}$ erg) agree well with Type IIb SNe, while moderate kinetic energies ($E_{\text{kin}} < 1.5 \times 10^{51}$ erg) agree well with Type Ib/c SNe. This result is in contrast with the expected kinetic energies of each type ([Kushnir 2015b](#), see). However, both progenitor models of [Yoon et al. \(2019\)](#) are a star stripped from its envelope through a binary companion, and the ejecta masses of these models are relatively low (see Appendix C). Type Ib/c SNe progenitors might be massive Wolf-Rayet (WR) stars ([Kushnir 2015b](#)), which can lead to a different range of ejecta masses and energies, so the lower t_0 values of the Type IIb SNe might be the result of lower ejecta mass and not larger kinetic energies.

[Dessart et al. \(2016\)](#) considered 29 profiles of five different models that simulated the explosion of the mass donor in a close-binary system. The profiles vary in M_{ej} , E_{kin} , and have two levels of ^{56}Ni mixing. The derived values of t_0 and n are shown as black symbols in Figure 9. These models span a larger range of t_0 values than the ones that have been observed. This can be understood by inspecting the ^{56}Ni mass-averaged column density of each model, which determines the value of t_0 ([Wygoda et al. 2019a](#)). For the models considered by [Dessart et al. \(2016\)](#), the two levels of ^{56}Ni mixing are very similar, such that t_0 is mainly determined by the column density of the ejecta

$$t_0 \propto \sqrt{\int \rho dv} \propto \frac{M_{\text{ej}}}{\sqrt{E_{\text{kin}}}} \propto \alpha, \quad (17)$$

where $\alpha \equiv \frac{M_{\text{ej}}/M_\odot}{\sqrt{E_{\text{kin}}/10^{51} \text{ erg}}}$.

The t_0 values of our sample, using the density profile of [Dessart et al. \(2016\)](#), correspond to ejecta with $2.1 \lesssim \alpha \lesssim 3.5$, while the full set of models have α -values within $1 \lesssim \alpha \lesssim 4$.

SN 1993J was modelled by [Blinnikov et al. \(1998\)](#), using a profile with $M_{\text{ej}} = 2.26 M_\odot$ and $E_{\text{kin}} = 1.32 \times 10^{51}$ erg, which corresponds to $\alpha \approx 2$. Using radiation transfer codes, [Blinnikov et al. \(1998\)](#) compared their models to the observed U , B and V magnitudes, and to the bolometric luminosity, from shock breakout to 120 d since explosion. They found good agreement with the bolometric light curve, and decent agreement with the individual magnitudes. We derived $t_0 \approx 57$ d (purple symbol in the figure), which is much lower than the observed value of SN 1993J (≈ 100 d).

We find that γ -ray transfer simulations can be used to

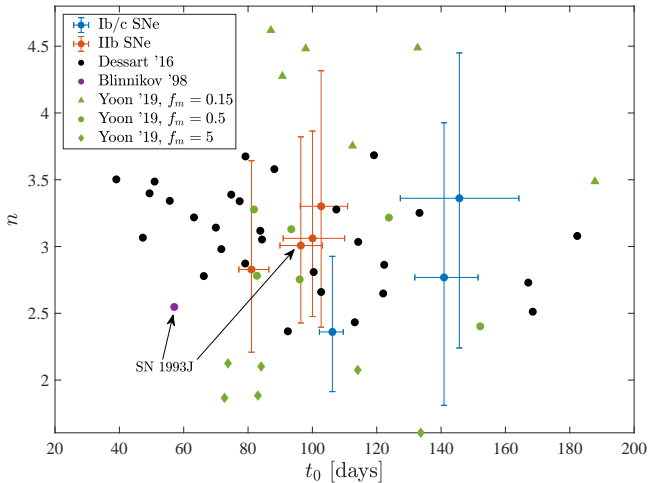


Figure 9. The $n - t_0$ distribution of SE SNe with relatively low t_0 error (blue and red), together with the MC γ -ray transfer results for the ejecta of Dessart et al. (2016, black), Blinnikov et al. (1998, purple), and Yoon et al. (2019, green symbols), the shape marks the degree of mixing).

constrain models in a number of ways. The observed range of t_0 is incompatible with models having too small or too large α values. This constrains the allowed range of masses and kinetic energies of the profiles, and indicates that the models of Dessart et al. (2016) with very small t_0 values of < 80 d are inconsistent with the observations. As can be seen in Appendix C, the level of ^{56}Ni mixing is portrayed in the value of n , where higher amount of mixing leads to lower n values. Although harder to determine, the n parameter of the observed SNe can be used to identify models with insufficient amount of ^{56}Ni mixing, like the profiles with low ^{56}Ni mixing of Yoon et al. (2019). Some of the models that are inconsistent with the observed γ -ray deposition were found to agree with optical observations. Since the optical radiation transfer calculations are more uncertain compared with the γ -ray transfer calculations, which are accurate and easy to implement, we believe that the observed γ -ray deposition provides a more robust constrain.

5.2 Type II SNe comparison with models – n and t_0

We apply the analysis of the previous section for Type II SN. The sample of Type II SNe with measured t_0 consists of SN 1987A, SN 2004et and SN 2017eaw. Since the optical depth for γ -rays does not become very small during the phases used for parameter fitting, there is a large degeneracy between t_0 and n (and an especially large uncertainty in n). The $n - t_0$ 68 per cent confidence region derived for these SNe are shown in Figure 10. Also shown are these parameters for several models from the literature, which include the blue supergiant (BSG) progenitor explosion models of Sukhbold et al. (2016), Blinnikov et al. (2000) and Dessart & Hillier (2019), and the red super-giants (RSG) progenitor models of Utrobin & Chugai (2009) and Hillier & Dessart (2019). The model parameters are calculated with the MC γ -ray transfer code for the ejecta profiles, kindly given to us by the authors of the papers.

The ejecta of Sukhbold et al. (2016), marked with blue circles, include four profiles with an initial progenitor zero-age-main-sequence (ZAMS) of $(16.2, 18.2, 19.2, 20.2) \times M_\odot$, evolved to pre-SN, and exploded with the calibration model W18 (see Sukhbold et al. 2016, for details), which was de-

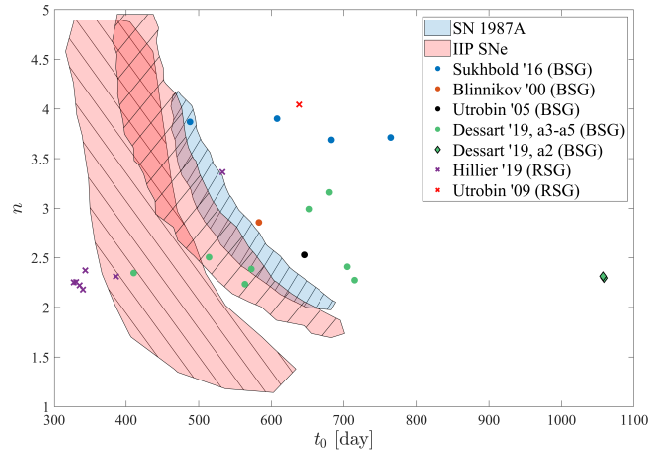


Figure 10. The $n - t_0$ 68% confidence region for the sample of Type II SNe with measured t_0 : SN 1987A (blue shaded region), SN 2004et and SN 2017eaw (both in red shaded region), together with the MC γ -ray transfer results for the ejecta of BSG (circles and diamonds) and RSG progenitors (crosses) from the literature. The BSG progenitors are of Sukhbold et al. (2016, blue circles), Blinnikov et al. (2000, red circle), Utrobin (2005, black circle), and Dessart & Hillier (2019, green circles for the a3,a4,a5 profiles and green diamonds for the a2 profiles). The RSG progenitors are of Hillier & Dessart (2019, purple crosses) and Utrobin & Chugai (2009, red cross).

signed to match the explosion parameters of SN 1987A. The t_0 values derived for the models with ZAMS solar masses of $(16.2, 18.2, 20.2)M_\odot$ match the observed t_0 of SN 1987A, while the derived t_0 of the $19.2M_\odot$ ZAMS model, which has a low explosion energy, is larger than the observed value. The relatively unmixed ^{56}Ni distribution of these profiles (see Appendix C) results in larger n values than the observed value.

Blinnikov et al. (2000) modelled the light curve of SN 1987A using $M_{\text{ej}} = 14M_\odot$ ejecta with various kinetic energies and isotope distributions. Using a radiation transfer code, Blinnikov et al. (2000) compared the monochromatic and bolometric light curves up to 180 d since explosion, and found a good match between the observations and the simulation. The derived value of t_0 and n (red symbol in the figure) for the profile that was provided (14E1, with $E_{\text{kin}} \approx 1.0 \times 10^{51}$ erg and a relatively mixed isotope distribution) is consistent with the observed values.

Utrobin (2005) constructed SN ejecta profiles to match the light curve of SN 1987A. We were given the $18M_\odot$ ejecta profile, which provided the best match to the light curve in the original work. This agreement with the observations also appears for the derived t_0 and n values (black symbol in the figure). Dessart & Hillier (2019) simulated the explosion of a $15M_\odot$ ZAMS star that collapsed as a BSG. The resulting ejecta (green symbols) have a range of M_{ej} , E_{kin} , and $M_{\text{Ni}56}$. The a3,a4,a5 profiles, shown in circles, have derived t_0 values in the range 400–700 d. The derived values of t_0 and n for the a4 profiles are consistent with the observed SN 1987A values, and are also the ones with the closest match to the early bolometric light curve in the original work. The a2 profiles, shown as diamonds (notice that there are two overlapping symbols), have small kinetic energies, and result in substantially large t_0 values of ≈ 1050 d, which is inconsistent with SN 1987A. They also substantially deviate from the early bolometric light curve in the original work.

Hillier & Dessart (2019) studied the explosions of an RSG evaluated from ZAMS mass of $15M_\odot$. Different values for the final mass of the star and different masses for possi-

ble circumstellar matter were considered. The range of ejecta mass was $\approx 11 - 13 M_{\odot}$. Hillier & Dessart (2019) compared the magnitude of individual bands and the spectra of their models, calculated with a radiation transfer code, to Type IIP SN observations. They found a good match between SN 2004et and the x1p5ext3 profile. The derived t_0 values (purple crosses) are relatively low compared with the observed Type IIP SNe, although some of them are consistent with $t_0 = 419^{+135}_{-47}$ of SN 2004et (and especially, the t_0 value of the x1p5ext3 profile is ≈ 380 d). Utrobin & Chugai (2009) modelled the light curve of SN 2004et with high $M_{\text{ej}} = 22.9 M_{\odot}$, which explains the large derived value $t_0 \approx 640$ d (red cross), compared with the observed t_0 of this SN. In the original work, the bolometric light curve of the model was calculated using a radiation transfer code and compared to the observed light curve from the explosion to 200 d since explosion, and resulted in a very good match.

Similar to other types of SNe, γ -ray transfer simulations of Type II SNe can discriminate models with t_0 values that are inconsistent with observations. In the case of Type II SNe, t_0 is hard to determine, often being larger than the last observed epoch. Nevertheless, models with low t_0 values, such as some of the RSG profiles of Hillier & Dessart (2019), are below all observed values or the lower limits of Type II SNe with observations exceeding 300 d since explosion. Additionally, the observed values of some specific SNe, such as SN 1987A and SN2004et, is inconsistent with some proposed ejecta, such as the high mass ejecta of Utrobin & Chugai (2009) that deviates from the observed value (despite the good match to the observed light curve in the original work). The parameter n and the amount of mixing is also much harder to determine than for SE SNe, but it is quite constraining for the case of SN 1987A. We find that the unmixed models of Sukhbold et al. (2016) do not fit SN 1987A and some mixing is required. This is supported by comparison to other observations as well (Blinnikov et al. 2000; Utrobin 2005).

5.3 Comparison with models – ET

Using the derived ET values and the analytical relations of Shussman et al. (2016), we can attempt to estimate the radius of the progenitor stars, R_* . In their work, the explosions of RSG progenitors were simulated, and the resulting ET values were compared with:

$$ET \approx \beta v_{\text{ej}} M_{\text{ej}} R_* \approx 1.5 \beta (E_{\text{exp}} M_{\text{ej}})^{1/2} R_*, \quad (18)$$

where E_{exp} is the explosion energy, M_{ej} is the ejected mass, $v_{\text{ej}} = \sqrt{2E_{\text{exp}}/M_{\text{ej}}}$ is the root mean square velocity of the ejecta, and β is a scaling parameter. They found that a constant value of $\beta = 0.1$ can describe the results of the simulations to 30 per cent accuracy for progenitors with large envelope masses, but for progenitors with small envelope masses the scaling parameter decreases as the envelope mass decreases (if envelope mass is considered instead of total mass, then low envelope mass progenitors can also be well approximated). Although Shussman et al. (2016) were focused on Type IIP SNe, we can use Equation (18) to estimate the characteristic progenitor radius for other types of SNe in our sample. For Type IIb SNe, we assume $v_{\text{ej}} \approx 4 - 7 \times 10^3 \text{ km s}^{-1}$, $M_{\text{ej}} \approx 3 - 6 M_{\odot}$ (corresponding to $E_{\text{exp}} \approx 1 - 1.5 \times 10^{51} \text{ erg}$) and $\beta = 0.01$. The β value roughly corresponds to the scaling factor of the low envelope mass progenitors of Shussman et al. (2016). We find that the Type IIb SNe of our sample with observed ET have progenitor star radii of $R_* \approx 250 - 450 R_{\odot}$. Previous studies found that the

progenitor of SN 1993J was a yellow supergiant with a radius of $\approx 600 R_{\odot}$ (Woosley et al. 1994; Piro 2015). This is in a rough agreement with our results given the large uncertainties. For SN 1987A, we keep the original value of $\beta = 0.1$, and assume $v_{\text{ej}} \approx 2.5 - 3.5 \times 10^3 \text{ km s}^{-1}$ and $M_{\text{ej}} \approx 12 - 18 M_{\odot}$ (corresponding to $E_{\text{exp}} \approx 1 - 1.5 \times 10^{51} \text{ erg}$). We find that the radius of the progenitor is $R_* \approx 38 - 60 R_{\odot}$. This is in agreement with the BSG progenitor of SN 1987A, with an estimated radius of $R \approx 43 \pm 14 R_*$ (Arnett et al. 1989). The procedure described above is not applicable for Type Ib/c SNe, for which the progenitors are expected to have very little hydrogen, and predicts much larger progenitor radii than expected.

We next compare the observed ET to the values predicted from the models in Sections 5.1 and 5.2. The ET values of the models are calculated by summing the internal energy of the ejecta profiles and multiplying with the time since explosion. This is only possible if the internal energies (or temperatures) and radii are provided at early enough times, such that the energy deposited from ^{56}Ni decay is small compared to the initial energy. Only the ejecta of the BSG progenitors of Dessart & Hillier (2019), given in ~ 1 d since explosion, satisfy this condition (the other profiles were provided at very late times, so even the derived upper limits on ET , see below, are not useful). The ET values of these ejecta are $0.5 - 1.7 \times 10^{54} \text{ erg s}$, which are somewhat lower than the observed value of SN 1987A, $1.8 - 4.2 \times 10^{54} \text{ erg s}$.

For all SE SNe ejecta profiles that we obtained, the energy deposited from ^{56}Ni decay is larger than the thermal energy at the times of the profiles, so we can only provide an upper limit for ET . For the SN 1993J profile of Blinnikov et al. (1998) the upper limit is $ET < 9.9 \times 10^{53} \text{ erg s}$, which is consistent with the observed value of this SN, $0.1 - 2.2 \times 10^{54} \text{ erg s}$. The upper limits for the SE SNe profiles of Dessart et al. (2016) are in the range of $ET < 0.8 - 5 \times 10^{53} \text{ erg s}$. These values are lower than the observed ET of our SE SNe sample. Confirmation of our measured values would thus place a stringent constrain on the models.

6 DISCUSSION AND CONCLUSIONS

We have constructed (Section 2) and analysed (Sections 3, 4) bolometric light curves to constrain the γ -ray deposition history of several types of SNe (Figure 1). We have recovered the tight range of γ -ray escape time, $t_0 \approx 30 - 45$ d, for Type Ia SNe (Wygoda et al. 2019a), and have been able to correct a small ≈ 10 per cent systematic error in the t_0 values of these SNe. We have found a new tight range $t_0 \approx 80 - 140$ d, where different subtypes of this class have quite similar t_0 values despite their different spectral characterization. Type Ib/c have slightly higher t_0 values compared with Type IIb, and a non-negligible ET value (Figure 6). We treat these ET measurements as tentative, since they could be an artifact of systematic errors. Type IIP SNe are clearly separated from other SNe types with $t_0 \gtrsim 400$ d, and there is a possible negative correlation between t_0 and the synthesized ^{56}Ni mass. We have found that the typical masses of the synthesized ^{56}Ni in SE SNe are larger than those in Type IIP SNe, in agreement with Kushnir (2015b), a fact that disfavors progenitors with the same initial mass range for these explosions (see detailed discussion in Kushnir 2015b). Instead, the progenitors of SE SNe explosions could be massive Wolf-Rayet stars, which are predicted to yield strong explosions with low ejecta masses according to the collapse-induced thermonuclear explosions mechanism for core-collapse SNe (Kushnir & Katz 2015; Kushnir 2015a,b).

We have applied a simple γ -ray radiation transfer code to calculate the γ -ray deposition histories of models from the literature (Section 5), and we have shown that the observed histories are a powerful tool to constrain models.

The sample of core-collapse SNe is quite limited, although in principle it is straightforward to increase the size of this sample. This would require a collaborated effort to acquire UV to IR coverage from early to late times, with the IR observation being of a special importance, reaching up to ~ 40 per cent at some phases. Accurate bolometric observations might help to determine the ET values of SE SNe, which would allow stringent constraints on the progenitor system. Additional Type IIP SNe might help determine whether t_0 and $M_{\text{Ni}56}$ are correlated, which would have consequences for the explosion mechanism.

ACKNOWLEDGEMENTS

We thank Boaz Katz, Nahliel Wygoda, Eran Ofek and Subo Dong for useful discussions. We thank Stan Woosley, Luc Dessart, Sung-Chul Yoon, Tuguldur Sukhbold, Sergei Blinnikov, and Victor P. Utrobin for sharing their ejecta profiles with us. DK is supported by the Israel Atomic Energy Commission –The Council for Higher Education –Pazi Foundation –and by a research grant from The Abramson Family Center for Young Scientists. The data underlying this article are available in the article and in its online supplementary material.

REFERENCES

- Anderson J. P., 2019, *A&A*, **628**, A7
- Arnett W. D., 1979, *The Astrophysical Journal*, **230**, L37
- Arnett W. D., 1982, *ApJ*, **253**, 785
- Arnett W. D., Bahcall J. N., Kirshner R. P., Woosley S. E., 1989, *ARA&A*, **27**, 629
- Axelrod T. S., 1980, PhD thesis, California Univ., Santa Cruz.
- Bianco F., et al., 2014, *The Astrophysical Journal Supplement Series*, **213**, 19
- Blinnikov S., Eastman R., Bartunov O., Popolitov V., Woosley S., 1998, *The Astrophysical Journal*, **496**, 454
- Blinnikov S., Lundqvist P., Bartunov O., Nomoto K., Iwamoto K., 2000, *The Astrophysical Journal*, **532**, 1132
- Branch D., Tammann G., 1992, *Annual review of astronomy and astrophysics*, **30**, 359
- Brown P. J., Breeveld A. A., Holland S., Kuin P., Pritchard T., 2014, *Ap&SS*, **354**, 89
- Brown P. J., Breeveld A., Roming P. W., Siegel M., 2016, *The Astronomical Journal*, **152**, 102
- Burns C. R., et al., 2018, *ApJ*, **869**, 56
- Chen J., et al., 2014, *The Astrophysical Journal*, **790**, 120
- Childress M. J., et al., 2015, *MNRAS*, **454**, 3816
- Churazov E., et al., 2014, *Nature*, **512**, 406
- Colgate S. A., McKee C., 1969, *The Astrophysical Journal*, **157**, 623
- Colgate S. A., Petschek A. G., Kriese J. T., 1980, *The Astrophysical Journal*, **237**, L81
- Contreras C., et al., 2018, *ApJ*, **859**, 24
- Dessart L., Hillier D. J., 2019, *Astronomy & Astrophysics*, **622**, A70
- Dessart L., Hillier D. J., Woosley S., Livne E., Waldman R., Yoon S.-C., Langer N., 2016, *Monthly Notices of the Royal Astronomical Society*, **458**, 1618
- Ergon M., et al., 2015, *Astronomy & Astrophysics*, **580**, A142
- Firth R. E., et al., 2015, *MNRAS*, **446**, 3895
- Fitzpatrick E. L., 1999, *Publications of the Astronomical Society of the Pacific*, **111**, 63
- Folatelli G., et al., 2014, *The Astrophysical Journal*, **792**, 7
- Fraser M., et al., 2011, *Monthly Notices of the Royal Astronomical Society*, **417**, 1417
- Friedman A. S., et al., 2015, *ApJS*, **220**, 9
- Ganeshalingam M., et al., 2010, *ApJS*, **190**, 418
- Graham M. L., et al., 2017, *MNRAS*, **472**, 3437
- Guillochon J., Parrent J., Kelley L. Z., Margutti R., 2017, *The Astrophysical Journal*, **835**, 64
- Hicken M., et al., 2009, *ApJ*, **700**, 331
- Hillier D. J., Dessart L., 2019, *Astronomy & Astrophysics*, **631**, A8
- Hunter D. J., et al., 2009, *Astronomy & Astrophysics*, **508**, 371
- Jeffery D. J., 1999, arXiv preprint astro-ph/9907015
- Junde H., 1999, *Nuclear Data Sheets*, **86**, 315
- Katz B., Kushnir D., Dong S., 2013, arXiv e-prints, p. [arXiv:1301.6766](https://arxiv.org/abs/1301.6766)
- Khatami D. K., Kasen D. N., 2019, *The Astrophysical Journal*, **878**, 56
- Krisciunas K., et al., 2017, *The Astronomical Journal*, **154**, 211
- Kushnir D., 2015a, arXiv e-prints, p. [arXiv:1502.03111](https://arxiv.org/abs/1502.03111)
- Kushnir D., 2015b, arXiv e-prints, p. [arXiv:1506.02655](https://arxiv.org/abs/1506.02655)
- Kushnir D., Katz B., 2015, *ApJ*, **811**, 97
- Kushnir D., Katz B., 2019, *Research Notes of the American Astronomical Society*, **3**, 162
- Kushnir D., Waxman E., 2020, Constraints on the density distribution of type Ia supernovae ejecta inferred from late-time light curves flattening ([arXiv:2001.10005](https://arxiv.org/abs/2001.10005))
- Kushnir D., Katz B., Dong S., Livne E., Fernández R., 2013, *ApJ*, **778**, L37
- Lyman J., Bersier D., James P., 2013, *Monthly Notices of the Royal Astronomical Society*, **437**, 3848
- Lyman J., Bersier D., James P., Mazzali P., Eldridge J., Fraser M., Pian E., 2016, *Monthly Notices of the Royal Astronomical Society*, **457**, 328
- Maguire K., et al., 2010, *Monthly Notices of the Royal Astronomical Society*, **404**, 981
- Matheson T., et al., 2012, *ApJ*, **754**, 19
- Matthews K., Neugebauer G., Armus L., Soifer B. T., 2002, *AJ*, **123**, 753
- Matz S., Share G., Leising M., Chupp E., Vestrandt W., Purcell W., Strickman M., Reppin C., 1988, *Nature*, **331**, 416
- Meza N., Anderson J. P., 2020, Stripped-envelope core-collapse supernova ^{56}Ni masses: Persistently larger values than supernovae type II ([arXiv:2002.01015](https://arxiv.org/abs/2002.01015))
- Milne P., Leising M., et al., 1999, *The Astrophysical Journal Supplement Series*, **124**, 503
- Milne P. A., Leising M. D., et al., 2001, *The Astrophysical Journal*, **559**, 1019
- Munari U., Henden A., Belligoli R., Castellani F., Cherini G., Righetti G. L., Vagnozzi A., 2013, *New Astron.*, **20**, 30
- Nakar E., Poznanski D., Katz B., 2016, *ApJ*, **823**, 127
- Pan Y. C., et al., 2015, *MNRAS*, **452**, 4307
- Pankey Titus J., 1962, PhD thesis, HOWARD UNIVERSITY.
- Pastorello A., et al., 2007a, *MNRAS*, **376**, 1301
- Pastorello A., et al., 2007b, *MNRAS*, **377**, 1531
- Pastorello A., et al., 2008, *Monthly Notices of the Royal Astronomical Society*, **389**, 955
- Pastorello A., et al., 2009, *Monthly Notices of the Royal Astronomical Society*, **394**, 2266
- Piro A. L., 2015, *The Astrophysical Journal Letters*, **808**, L51
- Prentice S., et al., 2016, *Monthly Notices of the Royal Astronomical Society*, **458**, 2973
- Prentice S. J., et al., 2018a, *MNRAS*, **478**, 4162
- Prentice S., et al., 2018b, *Monthly Notices of the Royal Astronomical Society*, **485**, 1559
- Rho J., Geballe T., Banerjee D., Dessart L., Evans A., Joshi V., 2018, *The Astrophysical Journal Letters*, **864**, L20
- Richmond M. W., Treffers R. R., Filippenko A. V., Paik Y., 1996, *AJ*, **112**, 732
- Ruiz-Lapuente P., Spruit H. C., 1998, *The Astrophysical Journal*, **500**, 360
- Sahu D. K., Anupama G., Sridvidya S., Muneer S., 2006, *Monthly Notices of the Royal Astronomical Society*, **372**, 1315
- Scalzo R., et al., 2014, *Monthly Notices of the Royal Astronomical Society*, **440**, 1498

- Scalzo R. A., et al., 2019, *MNRAS*, **483**, 628
- Seitenzahl I., Taubenberger S., Sim S., 2009, *Monthly Notices of the Royal Astronomical Society*, **400**, 531
- Shussman T., Nakar E., Waldman R., Katz B., 2016, arXiv e-prints, p. [arXiv:1602.02774](https://arxiv.org/abs/1602.02774)
- Silverman J. M., et al., 2012, *MNRAS*, **425**, 1789
- Stanishev V., et al., 2007, *A&A*, **469**, 645
- Stritzinger M., Leibundgut B., Walch S., Contardo G., 2006, *Astronomy & Astrophysics*, **450**, 241
- Stritzinger M., et al., 2018a, *Astronomy & Astrophysics*, **609**, A134
- Stritzinger M., et al., 2018b, *Astronomy & Astrophysics*, **609**, A135
- Sukhbold T., Ertl T., Woosley S., Brown J. M., Janka H.-T., 2016, *The Astrophysical Journal*, **821**, 38
- Suntzeff N. B., Bouchet P., 1990, *The Astronomical Journal*, **99**, 650
- Swartz D. A., Sutherland P. G., Harkness R. P., 1995, arXiv preprint astro-ph/9501005
- Szalai T., et al., 2019, *The Astrophysical Journal*, **876**, 19
- Taddia F., et al., 2018, *Astronomy & Astrophysics*, **609**, A136
- Takáts K., et al., 2013, *Monthly Notices of the Royal Astronomical Society*, **438**, 368
- Taubenberger S., et al., 2011, *Monthly Notices of the Royal Astronomical Society*, **413**, 2140
- Terreran G., et al., 2019, *ApJ*, **883**, 147
- Tomasella L., et al., 2013, *Monthly Notices of the Royal Astronomical Society*, **434**, 1636
- Tomita H., et al., 2006, *The Astrophysical Journal*, **644**, 400
- Tsvetkov D. Y., Pavlyuk N., Bartunov O., 2004, *Astronomy Letters*, **30**, 729
- Tsvetkov D. Y., Shugarov S. Y., Volkov I. M., Goranskij V. P., Pavlyuk N. N., Katyshcheva N. A., Barsukova E. A., Valeev A. F., 2013, *Contributions of the Astronomical Observatory Skalnaté Pleso*, **43**, 94
- Utrobin V., 2005, *Astronomy Letters*, **31**, 806
- Utrobin V., Chugai N., 2009, *Astronomy & Astrophysics*, **506**, 829
- Valenti S., et al., 2011, *Monthly Notices of the Royal Astronomical Society*, **416**, 3138
- Wheeler J. C., Johnson V., Clocchiatti A., 2015, *Monthly Notices of the Royal Astronomical Society*, **450**, 1295
- Woosley S. E., Eastman R. G., Weaver T. A., Pinto P. A., 1994, *ApJ*, **429**, 300
- Wygoda N., Elbaz Y., Katz B., 2019a, *MNRAS*, **484**, 3941
- Wygoda N., Elbaz Y., Katz B., 2019b, *MNRAS*, **484**, 3951
- Yoon S.-C., Chun W., Tolstov A., Blinnikov S., Dessart L., 2019, *ApJ*, **872**, 174
- Yoshii Y., et al., 2003, *The Astrophysical Journal*, **592**, 467
- Yuan F., et al., 2016, *Monthly Notices of the Royal Astronomical Society*, **461**, 2003
- Zhai Q., et al., 2016, *AJ*, **151**, 125
- Zhang J.-J., Wang X.-F., Bai J.-M., Zhang T.-M., Wang B., Liu Z.-W., Zhao X.-L., Chen J.-C., 2014, *AJ*, **148**, 1

APPENDIX A: THE CASE OF SN 2011DH

The Type IIb SN 2011dh is one of the best observed SE SN in the last decade. It has been under extensive observations for a period of 2 yr, from the UV to the medium IR (Ergon et al. 2015). Although IR observations are available up to ~ 400 d from explosion, our fitting procedure works well only up to ~ 150 d from explosion, with best-fitting parameters $M_{\text{Ni}56} \approx 0.059 M_{\odot}$, $t_0 \approx 100$ d and $n \approx 2.8$, well within the range of Type IIb typical values (see Table 1). At later epochs, the optical flux declines faster than the well-observed Type IIb SN 1993J and SN 2008ax (Ergon et al. 2015), and so the bolometric luminosity declines faster as well. Applying the fitting procedure for the entire time range results in a very poor fit, with an extremely high value of the $n \approx 9$, far beyond any other SNe (see Figure A1). Ergon et al. (2015) suggested that dust formation in the ejecta might cause this

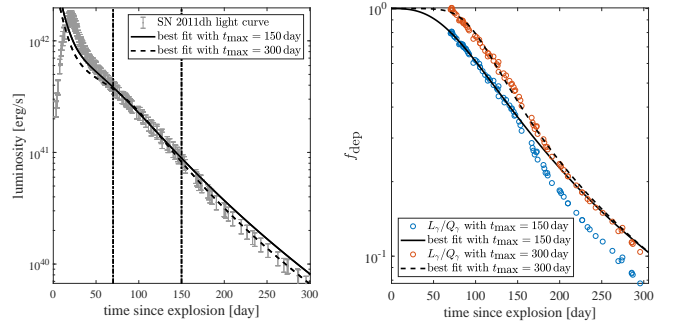


Figure A1. Same as Figure 5, for the case of SN 2011dh, comparing the best-fitting results of the shortened time range, $t_{\text{max}} = 150$ d, and the usual time range of SE SNe, $t_{\text{max}} = 300$ d (starting from $t_{\text{min}} = 70$ d). left-hand side panel: the observed bolometric light curve (grey symbols), the best-fitting model with the shortened time range (solid black line) and the best-fitting model with the usual time range (dashed line). The vertical dotted lines indicate t_{min} of both time ranges and t_{max} of the shortened time range. right-hand side panel: the γ -ray deposition fraction L_{γ}/Q_{γ} for the shortened time range (blue symbols), its best-fitting deposition model (solid line), the deposition fraction for the usual time range (orange symbols) and its best-fitting deposition model (dashed line).

phenomenon, supported by the fractional increase of the mid-IR luminosity at these epochs. In this scenario, the missing energy is emitted in wavelengths above the *Spitzer* $4.5 \mu\text{m}$ band, and are not taken into account.

APPENDIX B: BOLOMETRIC LIGHT CURVES AND THE RESULTS OF THE INTEGRAL METHOD FOR THE ENTIRE SAMPLE

We present here, in Fig. B1, the best-fitting bolometric light curves and the results of the integral method for the entire sample, in the same format as in Figure 5. The order is the same as in Table 1: Type Ia, Type Ib/c, Type IIb, Type IIP and, finally, SN 1987A.

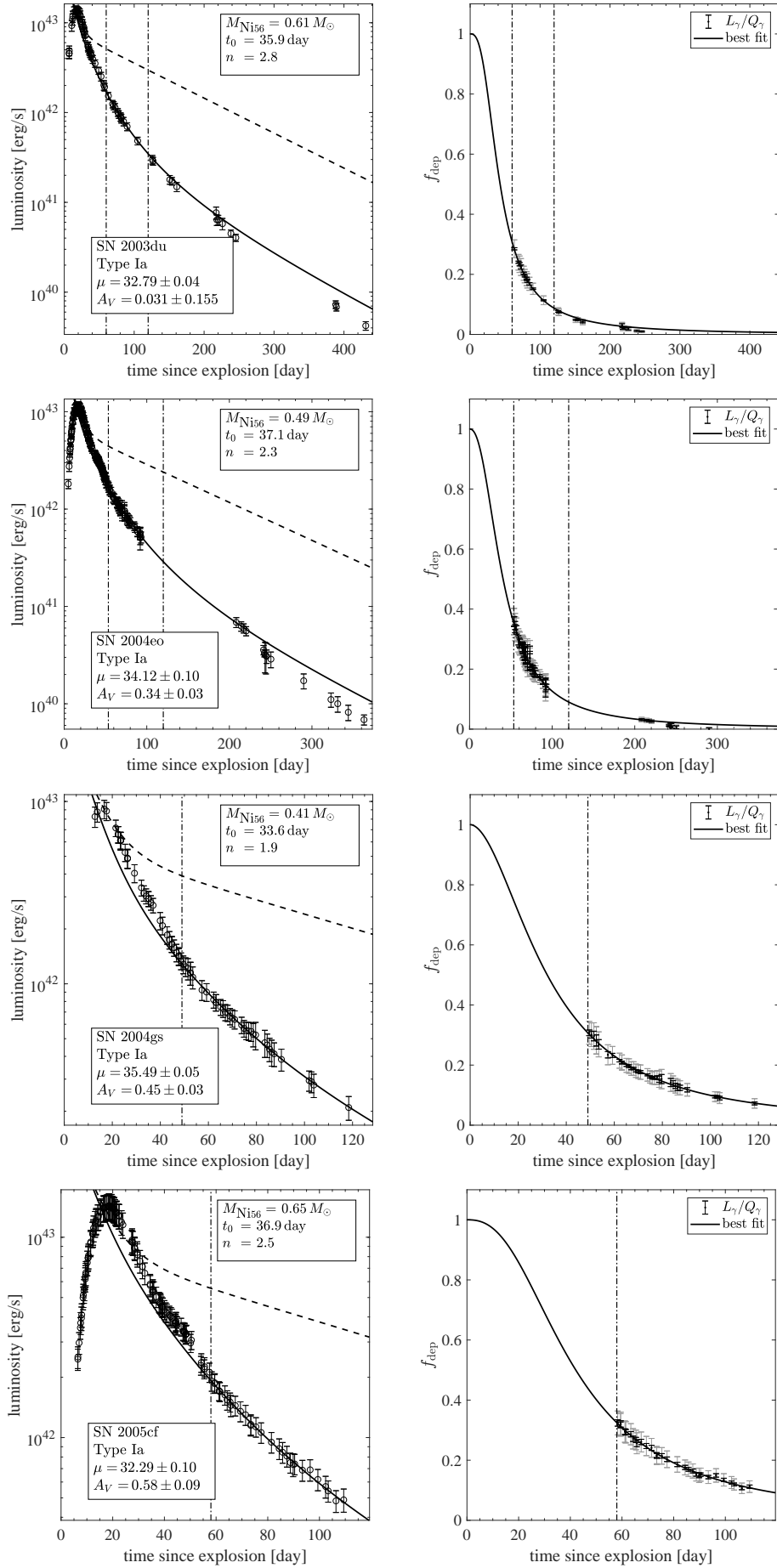


Figure B1. Same as Figure 5 for the full SNe sample.

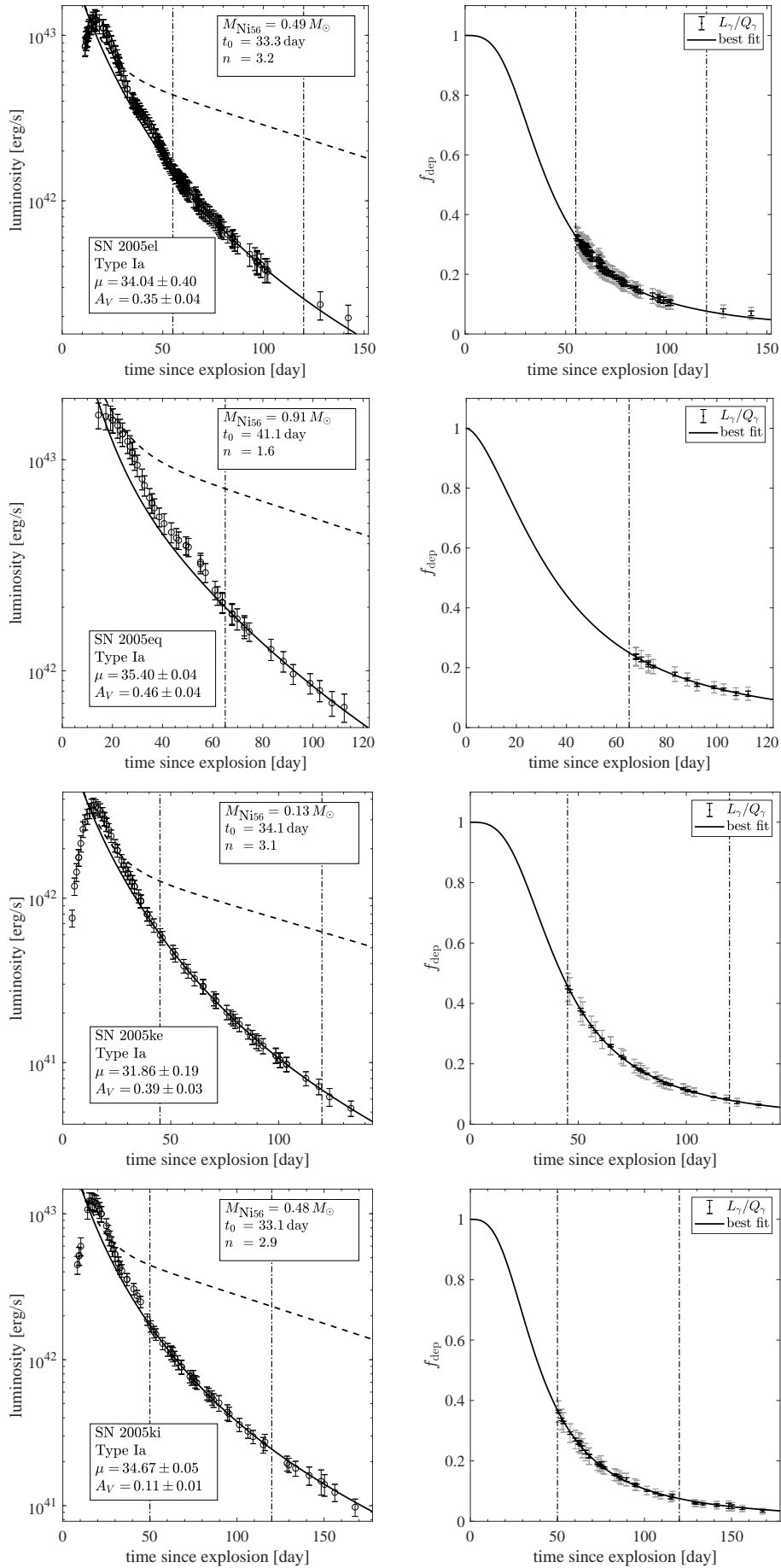


Figure B1. (continued) Same as Figure 5 for the full SNe sample.

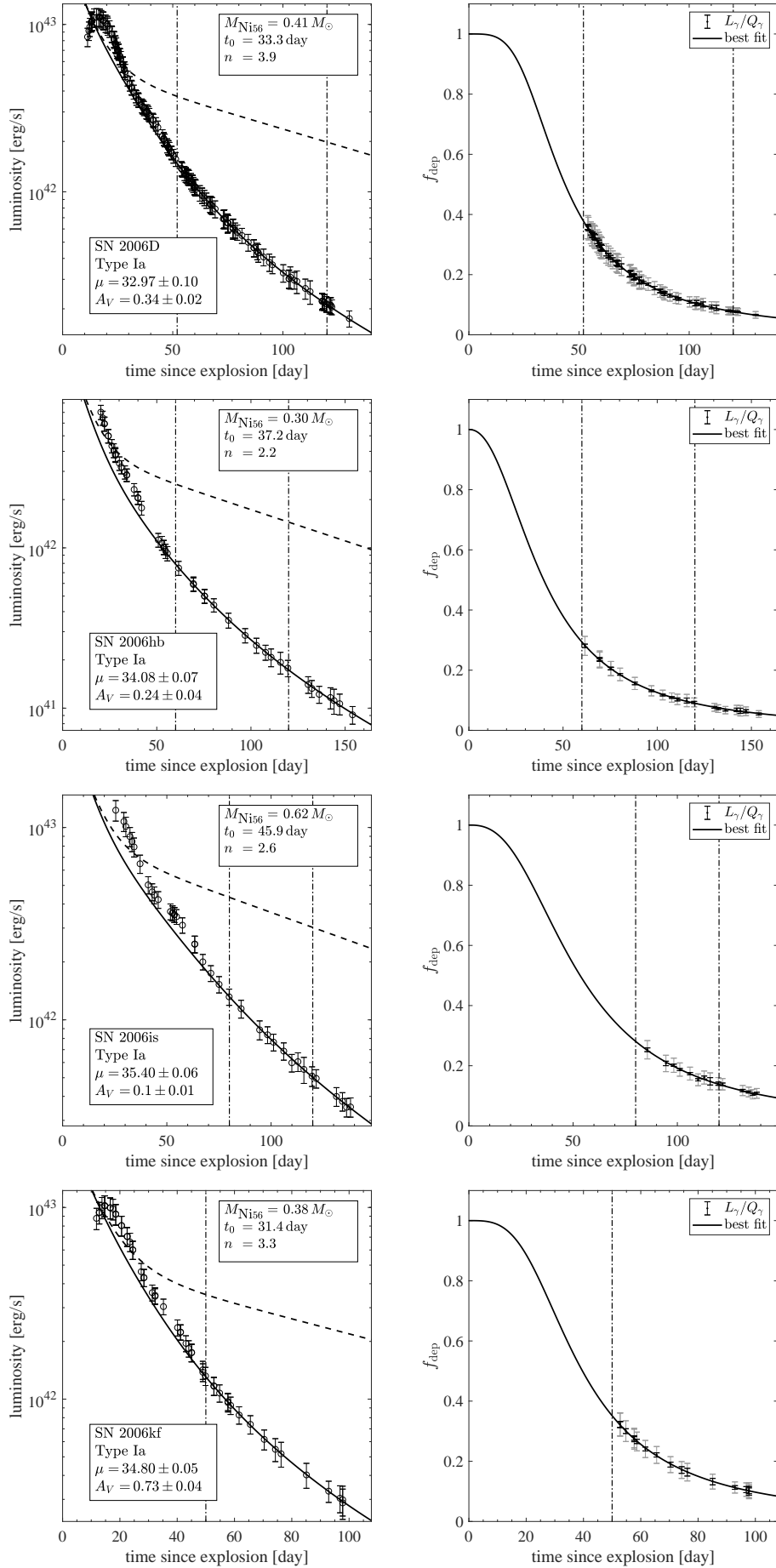


Figure B1. (continued) Same as Figure 5 for the full SNe sample.

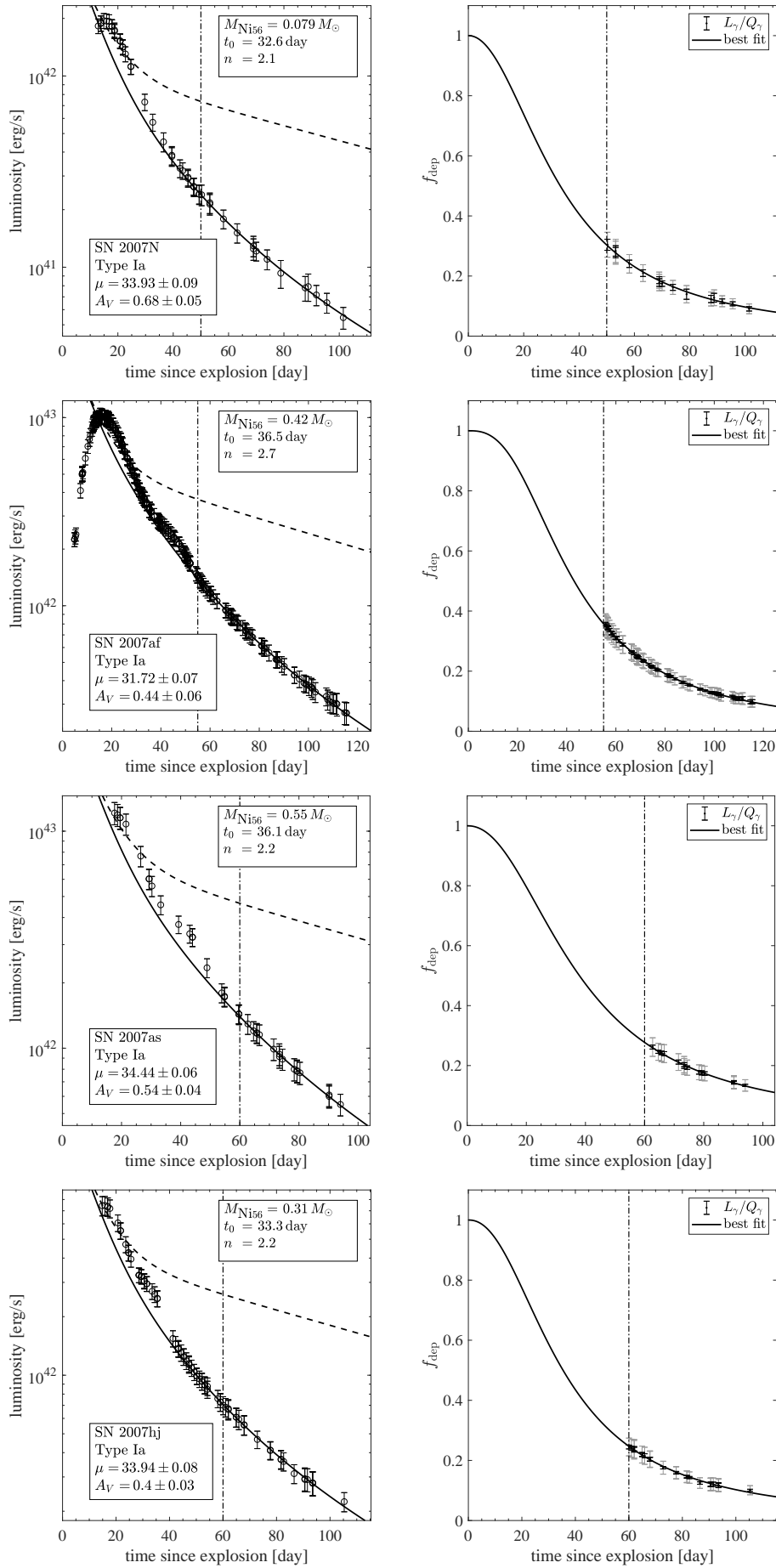


Figure B1. (continued) Same as Figure 5 for the full SNe sample.

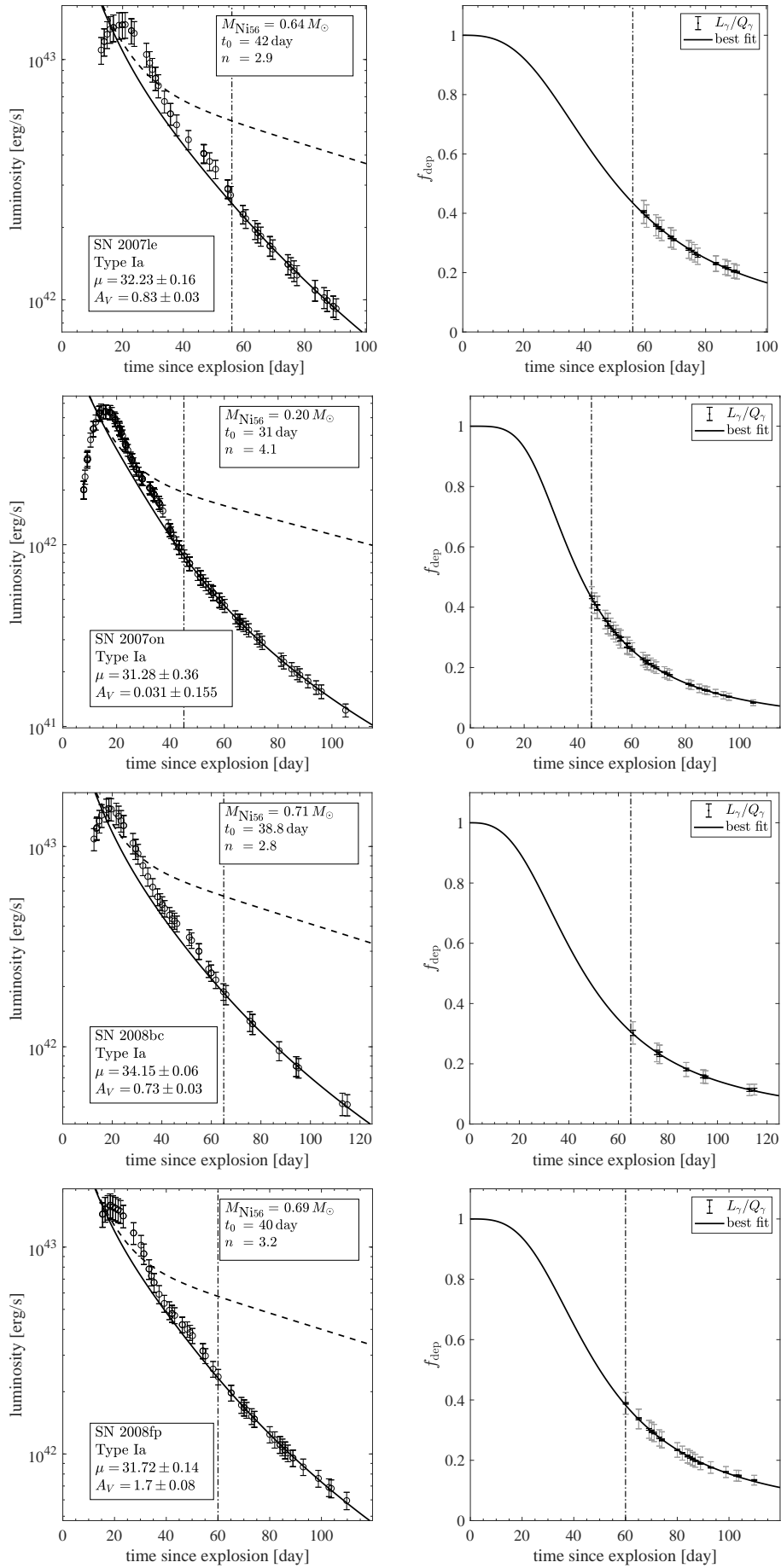


Figure B1. (continued) Same as Figure 5 for the full SNe sample.

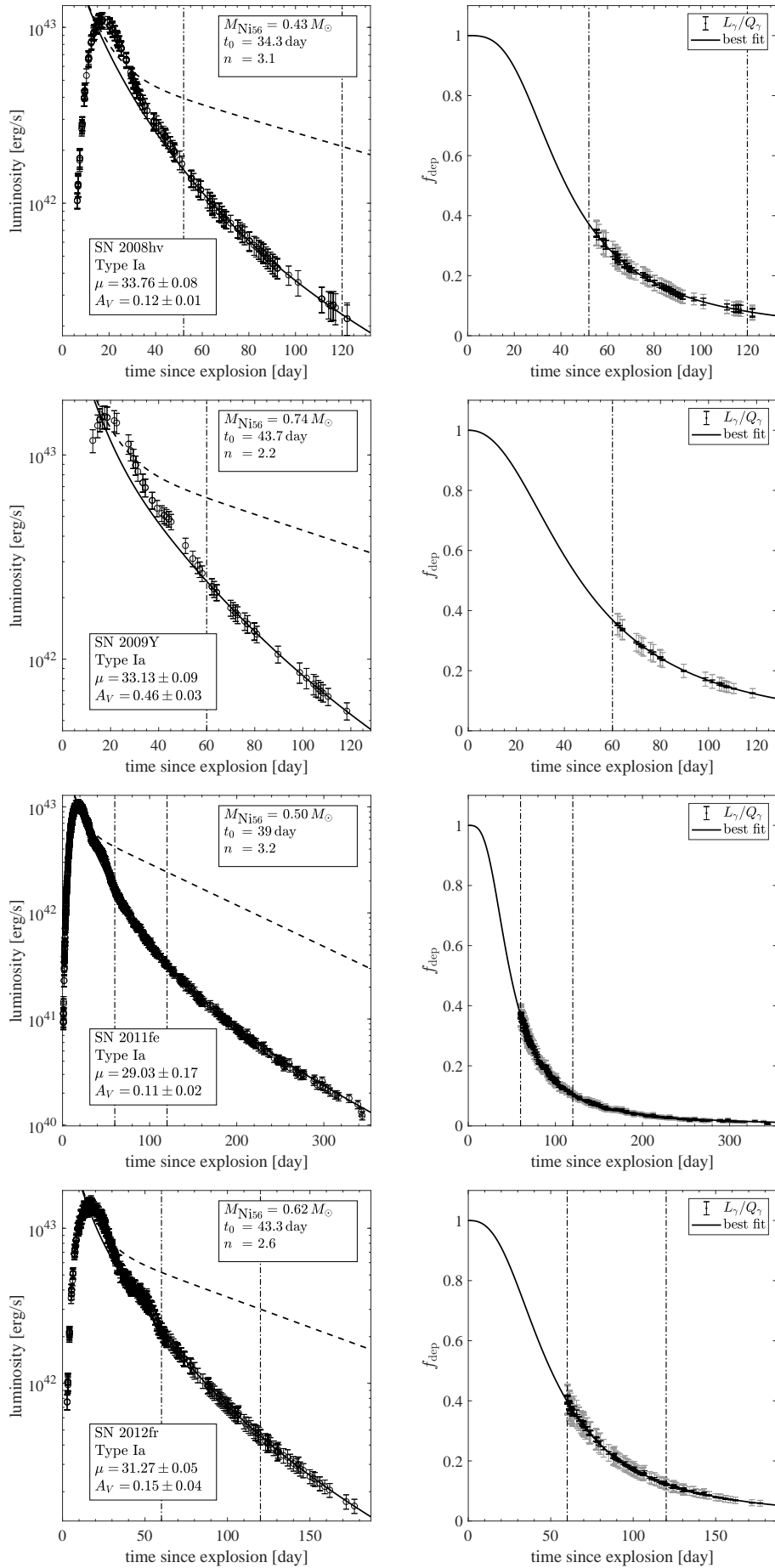


Figure B1. (continued) Same as Figure 5 for the full SNe sample.

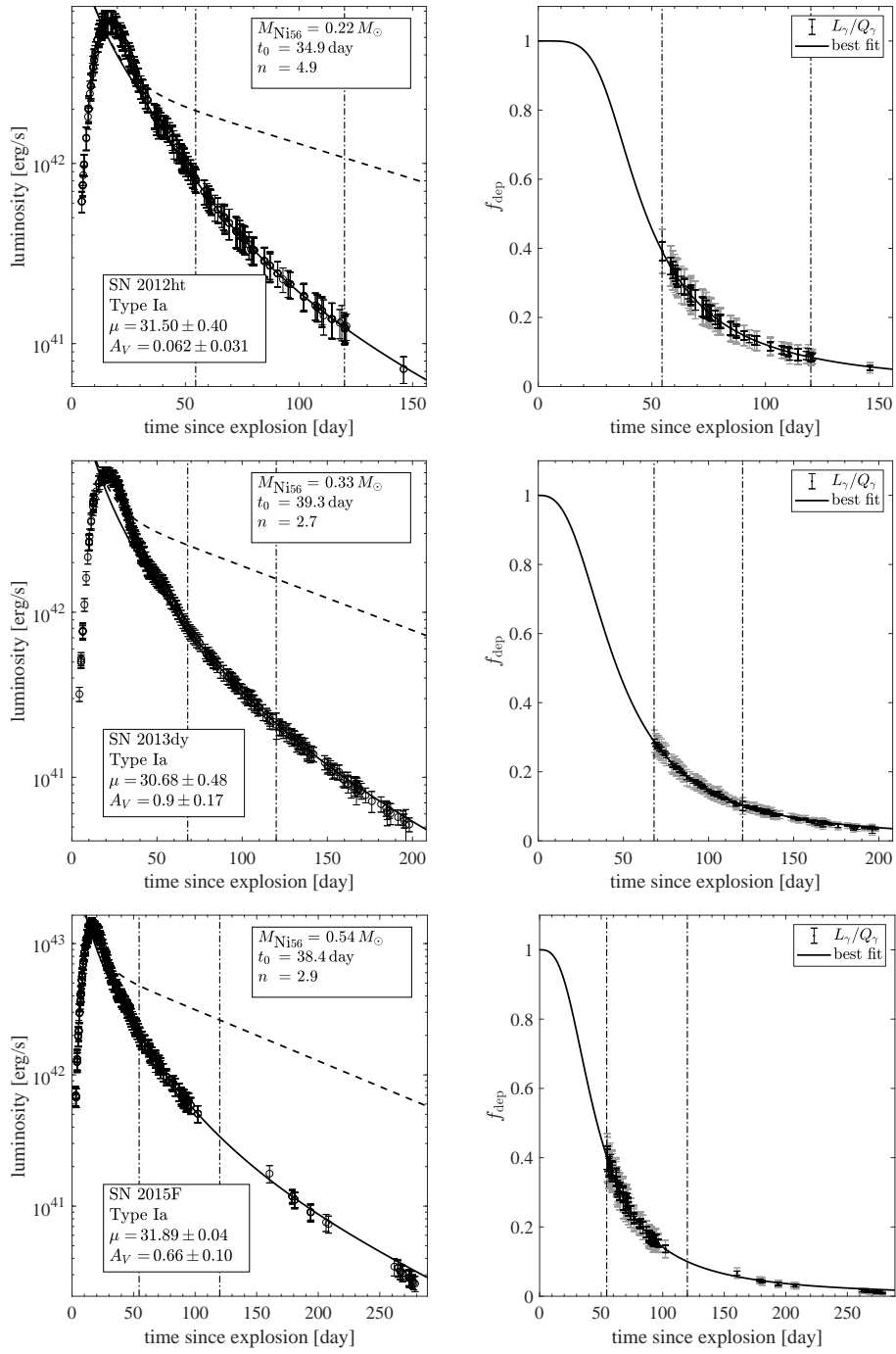


Figure B1. (continued) Same as Figure 5 for the full SNe sample.

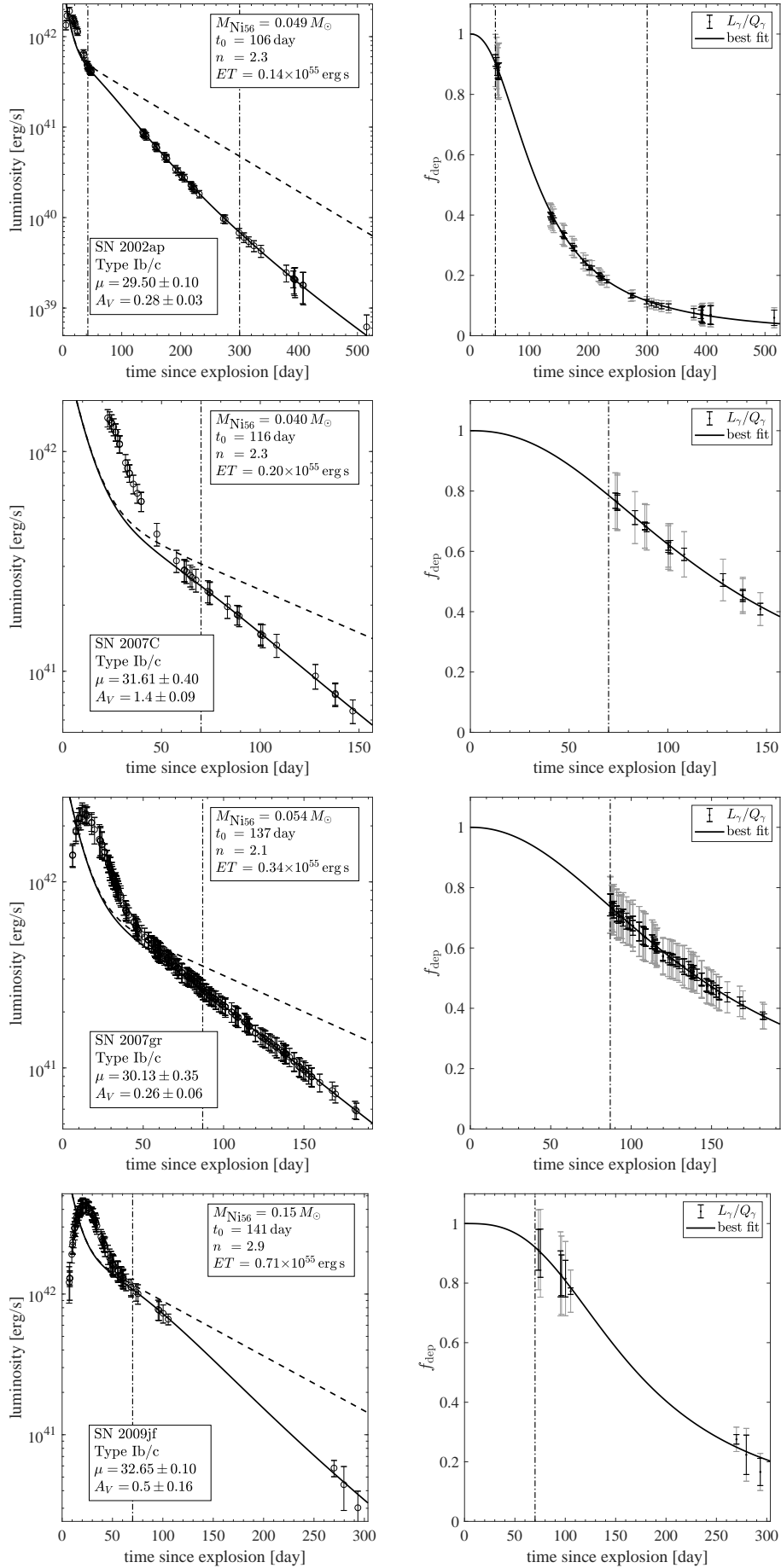


Figure B1. (continued) Same as Figure 5 for the full SNe sample.

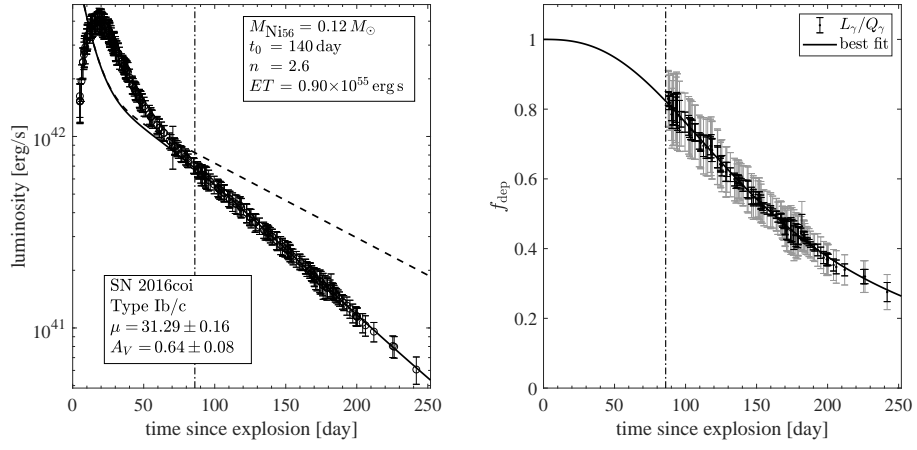


Figure B1. (continued) Same as Figure 5 for the full SNe sample.

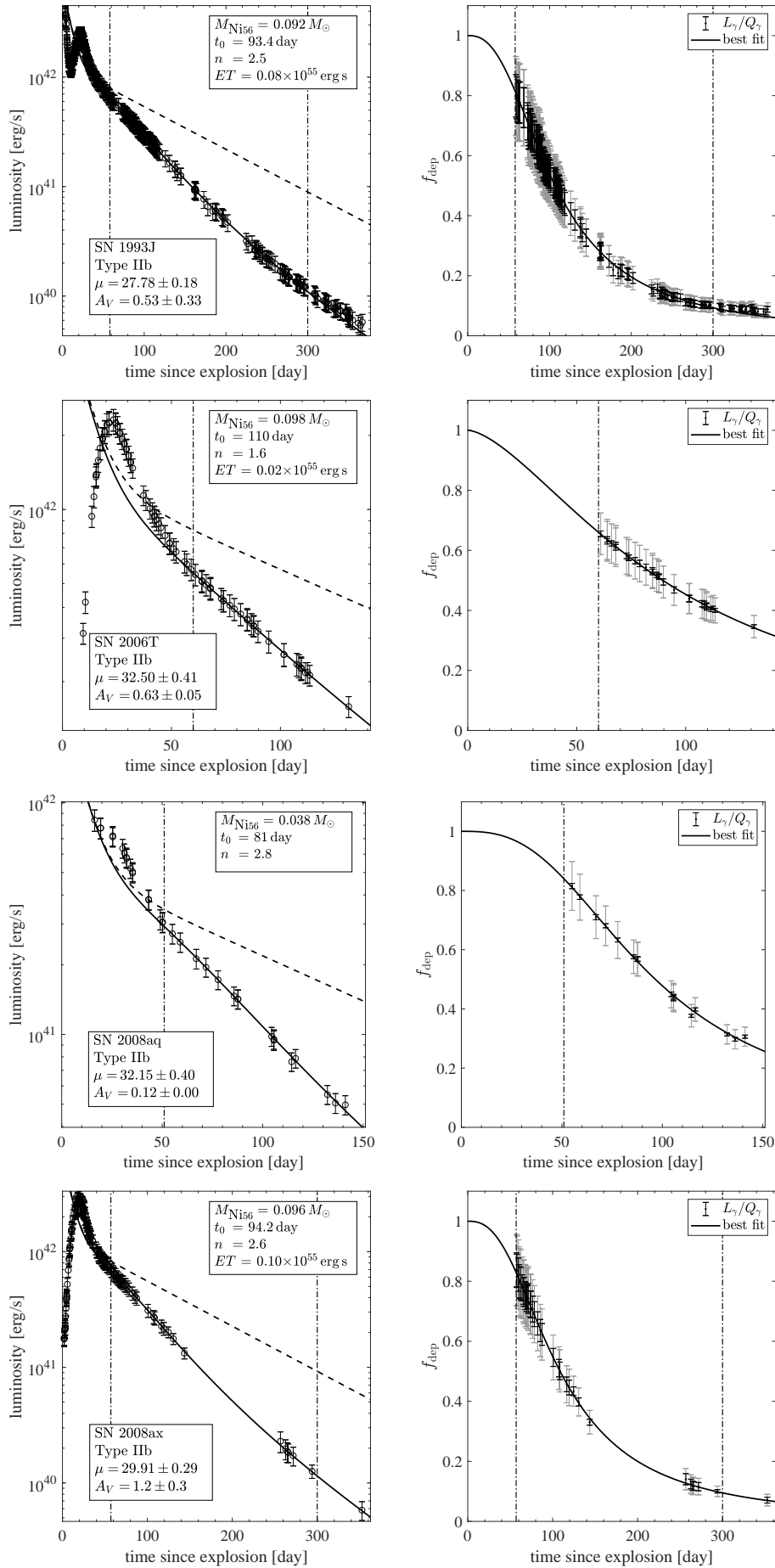


Figure B1. (continued) Same as Figure 5 for the full SNe sample.

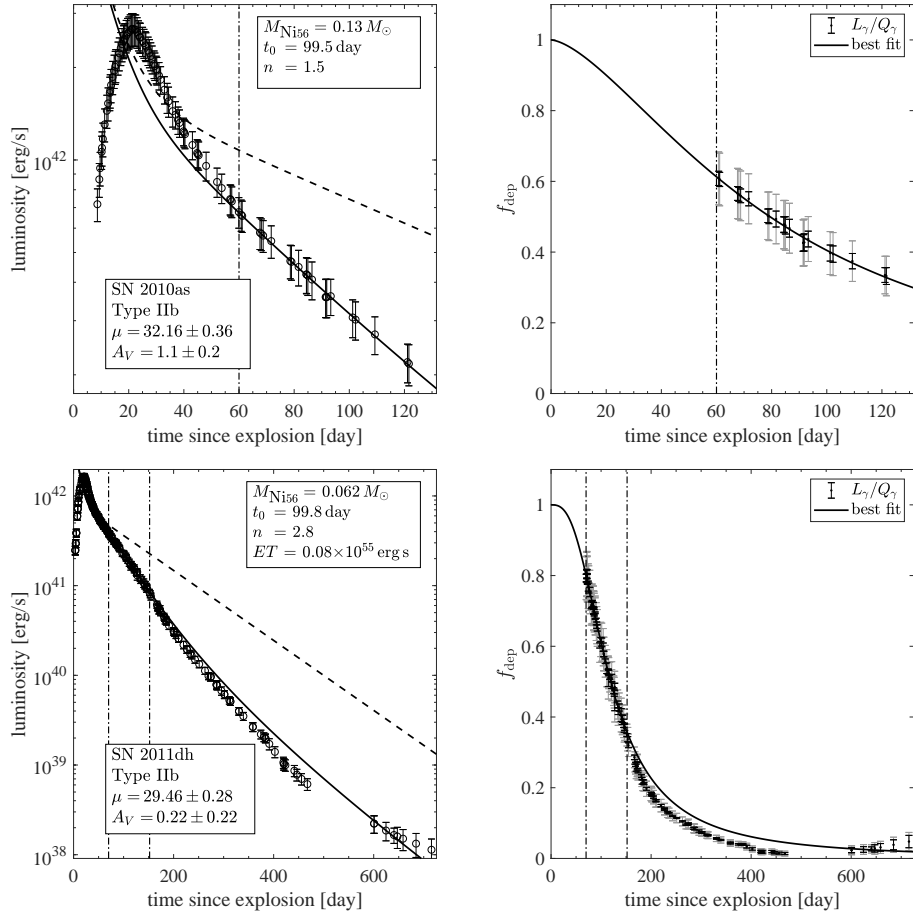


Figure B1. (continued) Same as Figure 5 for the full SNe sample.

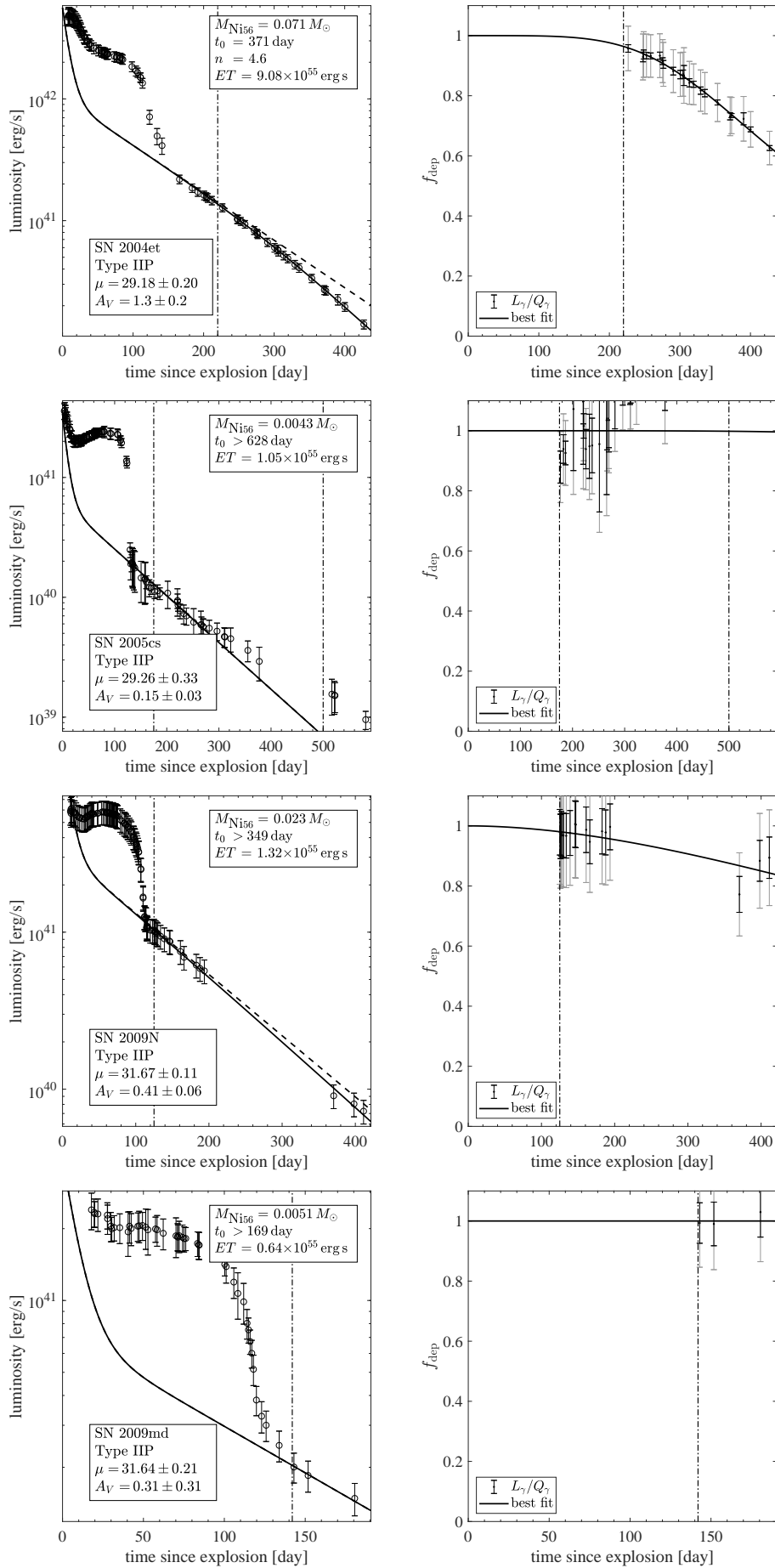


Figure B1. (continued) Same as Figure 5 for the full SNe sample.

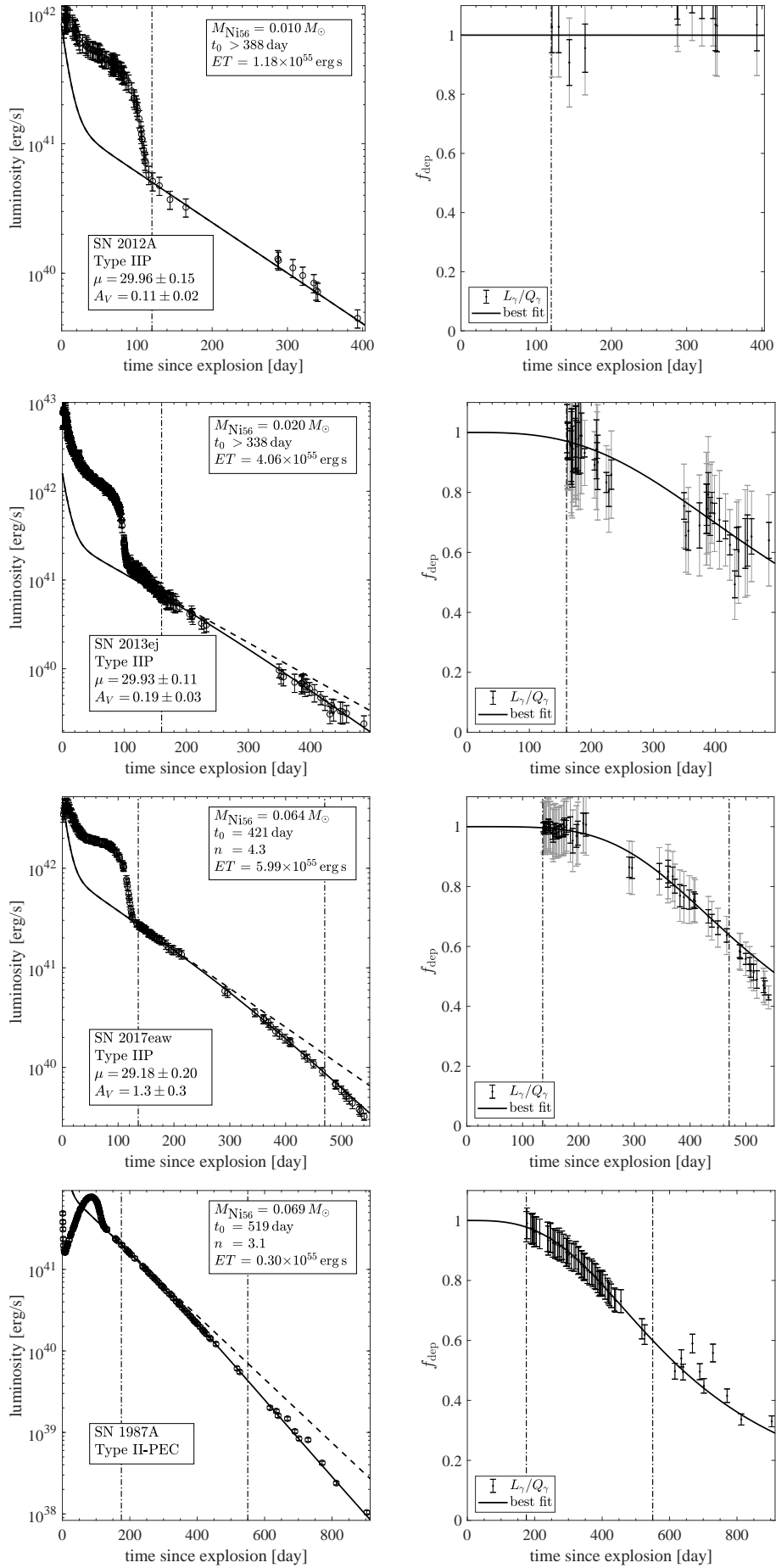


Figure B1. (continued) Same as Figure 5 for the full SNe sample.

APPENDIX C: MODEL PARAMETERS AND γ -RAY SIMULATION RESULTS

A summary of the models that were used in our γ -ray analysis and along with the results of the calculations is provided in Table C. We provide for each model the ejecta mass, the total kinetic energy of the ejecta, the amount of ^{56}Ni mixing as defined in Equation (16), and the ratio of the mass to the square root of kinetic energy, Equation (17).

Name	Type	$M_{\text{ej}} (M_{\odot})$	$E_{\text{kin}} (10^{51} \text{ erg})$	^{56}Ni mixing ^a	α^b	simulation t_0	simulation n	ref. ^c
HE3.87_fm0.15_E1.0	SE	2.4	0.67	0.087	2.93	132	4.5	1
HE3.87_fm0.5_E1.0	SE	2.4	0.67	0.28	2.93	123	3.2	1
HE3.87_fm5.0_E1.0	SE	2.4	0.67	0.50	2.93	114	2.1	1
HE3.87_fm0.15_E1.5	SE	2.4	1.17	0.087	2.22	97	4.5	1
HE3.87_fm0.5_E1.5	SE	2.4	1.17	0.28	2.22	93	3.1	1
HE3.87_fm5.0_E1.5	SE	2.4	1.17	0.50	2.22	84	2.1	1
HE3.87_fm0.15_E1.8	SE	2.4	1.47	0.087	1.98	87	4.6	1
HE3.87_fm0.5_E1.8	SE	2.4	1.47	0.28	1.98	81	3.3	1
HE3.87_fm5.0_E1.8	SE	2.4	1.47	0.50	1.98	73	2.1	1
CO3.93_fm0.15_E1.0	SE	2.49	0.53	0.087	3.42	187	3.5	1
CO3.93_fm0.5_E1.0	SE	2.49	0.53	0.28	3.42	152	2.4	1
CO3.93_fm5.0_E1.0	SE	2.49	0.53	0.50	3.42	133	1.6	1
CO3.93_fm0.15_E1.55	SE	2.49	0.99	0.087	2.5	112	3.8	1
CO3.93_fm0.5_E1.5	SE	2.49	0.99	0.28	2.5	96	2.8	1
CO3.93_fm5.0_E1.5	SE	2.49	0.99	0.50	2.5	83	1.9	1
CO3.93_fm0.15_E1.8	SE	2.49	1.27	0.087	2.21	90	4.3	1
CO3.93_fm0.5_E1.8	SE	2.49	1.27	0.28	2.21	82	2.8	1
CO3.93_fm5.0_E1.8	SE	2.49	1.27	0.50	2.21	72	1.9	1
he4p96Ax1	SE	3.54	1.25	0.14	3.16	133	3.3	2
he4p96Ax2	SE	3.62	1.29	0.3	3.18	122	2.6	2
he4p96Bx1	SE	3.61	2.49	0.088	2.29	88	3.6	2
he4p96Bx2	SE	3.63	2.49	0.22	2.3	84	3.1	2
he5p1Gx2	SE	3.65	5.4	0.13	1.57	63	3.2	2
he6p5Ax1	SE	4.98	1.26	0.2	4.43	182	3.1	2
he6p5Ax2	SE	4.97	1.26	0.35	4.43	168	2.5	2
he6p5Bx1	SE	4.95	2.43	0.12	3.18	119	3.7	2
he6p5Bx2	SE	4.98	2.43	0.27	3.19	114	3	2
he6p5Gx1	SE	5.14	5.29	0.087	2.24	79	3.7	2
he6p5Gx2	SE	5.18	5.3	0.2	2.25	77	3.3	2
3p0Ax1	SE	1.73	1.25	0.11	1.55	70	3.1	2
3p0Ax2	SE	1.72	1.24	0.19	1.54	66	2.8	2
3p0Bx2	SE	1.73	2.5	0.14	1.09	47	3.1	2
3p0Cx1	SE	1.71	0.62	0.15	2.17	100	2.8	2
3p0Cx2	SE	1.71	0.62	0.26	2.16	92	2.4	2
3p65Ax1	SE	2.23	1.24	0.14	2	84	3.1	2
3p65Ax2	SE	2.22	1.22	0.25	2.01	79	2.9	2
1993J_13C	SE	2.26	1.32	0.12	1.97	57	2.5	3
s16.2	II-pec	11.9	0.79	0.072	13.3	683	3.7	4
s18.2	II-pec	13.2	1.25	0.065	11.8	608	3.9	4
s19.2	II-pec	13.8	0.77	0.062	15.7	765	3.7	4
s20.2	II-pec	14.2	1.75	0.06	10.8	488	3.9	4
1987A_14E1	II-pec	14.7	1.06	0.26	14.2	583	2.9	5
1987A_M18	II-pec	18.1	1.50	0.21	14.8	645	2.5	6
a2	Type II-pec	14.3	0.47	0.3	20.9	1059	2.3	7
a2vth	Type II-pec	14.3	0.47	0.3	20.9	1057	2.3	7
a3	Type II-pec	13.5	0.87	0.29	14.5	705	2.4	7
a3m1	Type II-pec	12.5	0.87	0.17	13.5	652	3	7
a3m2	Type II-pec	12.5	0.87	0.096	13.5	680	3.2	7
a3ni	Type II-pec	13.4	0.87	0.31	14.4	715	2.3	7
a4	Type II-pec	13.2	1.26	0.29	11.8	573	2.4	7
a4he	Type II-pec	13.2	1.25	0.3	11.8	564	2.2	7
a4ni3	Type II-pec	12.6	1.26	0.31	11.2	514	2.5	7
a5	Type II-pec	13.1	2.46	0.3	8.36	410	2.3	7
15M_mdod1p5	II	12.1	1.23	0.12	10.9	533	3.4	8
15M_mdod3p0_e1pm0	II	13.2	1.19	0.49	12.1	386	2.3	8
15M_mdod3p0_e1pm1	II	11.1	1.28	0.48	9.84	340	2.2	8
15M_mdod3p0_e3pm1	II	11.3	1.30	0.48	9.91	330	2.3	8
15M_mdod3p0_e5pm1	II	11.6	1.36	0.48	9.96	327	2.3	8
15M_mdod3p0_e5pm2	II	11.1	1.28	0.48	9.82	335	2.2	8
15M_mdod3p0_e7pm1	II	12.1	1.28	0.48	10.7	343	2.4	8

Name	Type	$M_{\text{ej}} [M_{\odot}]$	$E_{\text{kin}} [10^{51} \text{ erg}]$	^{56}Ni mixing ^a	α^{b}	simulation t_0	simulation n	ref. ^c
2004et	II	22.9	2.23	0.017	15.3	638	4	9

^a ^{56}Ni mixing, see Equation (16).

^b The ratio of the ejecta mass to the square root of the kinetic energy (Equation 17).

^c The references are: 1. [Yoon et al. \(2019\)](#) 2. [Dessart et al. \(2016\)](#) 3. [Blinnikov et al. \(1998\)](#) 4. [Sukhbold et al. \(2016\)](#) 5. [Blinnikov et al. \(2000\)](#) 6. [Utrobin \(2005\)](#) 7. [Dessart & Hillier \(2019\)](#) 8. [Hillier & Dessart \(2019\)](#) 9. [Utrobin & Chugai \(2009\)](#).

This paper has been typeset from a $\text{\TeX}/\text{\LaTeX}$ file prepared by the author.